Hindawi
International Journal of Aerospace Engineering
Volume 2023, Article ID 9088200, 22 pages
https://doi.org/10.1155/2023/9088200

Research Article

Characteristics of Flow Development and Boiling Transitions in the Liquid Oxygen Chill-Down Process in a Straight Horizontal Exit-Contracted Pipe

Lanwei Chen and Jiaqi Zhang

Science and Technology on Scramjet Laboratory, College of Aerospace Science and Engineering, National University of Defense Technology, Changsha 410073, China

Correspondence should be addressed to Jiaqi Zhang; amatyer_a@hotmail.com

Received 21 September 2022; Revised 12 October 2022; Accepted 24 November 2022; Published 7 February 2023

Academic Editor: Yiheng Tong

Liquid oxygen chill-down in a straight horizontal pipe was studied experimentally. The effect of the entrance corner was excluded, and much denser wall temperature sensors along the pipe have been set compared to the present studies. In this way, the chill-down process, as well as the development of the flow pattern, has been drawn for every test. As a result, the mechanism of LO_2 chill-down would be obtained for various pressure sections. For cases with stable pressure below 1.25 MPa, liquid rewetting in the pipe is controlled by the propagation of quenching fronts. For cases with a higher pressure, liquid rewetting in the second half of the pipe is controlled by the sudden liquid fill-in. Based on the transition points obtained, heat transfer coefficients on the Leidenfrost point and critical heat flux have been correlated for various pressure sections using new approaches. Conclusions show that the correlation equations are dependent on the chill-down mechanisms.

1. Introduction

Cryogenic nontoxic liquid rocket engine is a hot spot in aerospace power development, such as liquid oxygen/kerosene and liquid oxygen/methane engine [1, 2]. A cryogenic propellant has the characteristics of a low boiling point and low latent heat of evaporation, so it is easy to boil into a two-phase flow, resulting in an uncontrollable flow process. The chill-down process reduces the temperature of the pipeline system below the saturation temperature of the cryogenic propellant. For example, when the rocket engine is fired, it can ensure that the propellant flow in the pipeline rapidly changes from the gas phase to the liquid phase [3]. The chilling determines the spray characteristics of the engine injector and directly affects the engine starting process [4]. During the chill-down process, the temperature of the pipeline system drops sharply to obtain the chilling, and the cryogenic propellant completes the filling of the pipeline and establishes steady flow. In this process, the cryogenic propellant usually crosses several boiling transition points and finally turns into the liquid phase, experiencing film boiling, transition boiling, and nuclear boiling [5–7].

According to the different structure of the pipe exit, the filling process can be divided into the pipeline filling with the exit-closed, the exit-open, and the exit-contracted. The last type of pipeline filling has less related research but more research value. Normal temperature propellant does not involve strong heat exchange and phase change for pipeline filling. Zhou et al. [8, 9] studied the contracted standpipe and horizontal pipe at the end of water filling which show that the rapid filling process is dominated by gas-liquid two-phase interaction, resulting in strong water shock pressure oscillation, and high heat can be generated by instantaneous air compression in some conditions. The chill-down process of the cryogenic pipeline system with exit-contracted involves the intense heat transfer between the cryogenic propellant and the thermal pipeline, which leads to phase transition. It involves the coupling of filling and chilling processes, and the physical process is more complex.

At present, a series of studies have been carried out on the chilling of cryogenic pipelines. Jin et al. [10–13] carried out a series of liquid nitrogen tests and simulation studies on long pipelines and proposed some heat transfer correlations. Hu et al. [14] carried out the observation of liquid oxygen chilling flow patterns in 8 mm vertical pipelines and captured several flow patterns and developments of the quenching front. Darr et al. [15–17] conducted a series of liquid nitrogen cooling pipeline tests, gave the influence law of pressure and flow parameter changes on heat flow and heat transfer coefficient at the boiling transition point, and proposed a series of correlation equations to predict T_{LFP} and q_{CHF}. Wang et al. [18, 19] carried out one-dimensional pipeline simulation research based on the existing heat transfer correlation and also studied the two-phase flow instability phenomenon in the liquid oxygen chilling process of long-distance pipeline transportation. Wang et al. [20] studied the influence of an inner microribbed pipeline, which showed that the structure enhanced the heat transfer at the film boiling stage and reduced the chilling time by half compared with the ordinary pipeline. Xu et al. [21, 22] studied the influence of coating materials on the chilling process. Chung et al. [6] studied the effect of pulse flow on the chilling process. Hartwig et al. [23] carried out tests with large pipe diameters for liquid oxygen and liquid methane. Darr et al. [24] presented one-dimensional simulation results of liquid nitrogen chilling in vertical pipelines, and the deviation between simulation and test results was within 25%. Chen et al. [25] conducted a CFD simulation study on the film boiling process in the chilling process of cryogenic pipeline and showed the distribution of cross-sectional flow patterns. Related chilling studies further revealed the heat transfer mechanism of the pipeline chilling process, but these studies usually have no contracted element on the pipeline exit, and low-pressure-drop elements are connected downstream of the pipeline. Because the overall pressure in the pipe is low (the pressure in the pipe is usually less than 1 MPa), the cryogenic propellant will be a two-phase flow state near the pipe outlet under some low-pressure conditions.

There are few studies on the chill-down process of pipeline exit-contracted. Corresponding actual scenarios include the following: During the engine hot-fire test, the propellant enters the rear pipeline from the main valve and reaches the combustor, and there is an injector at the end of the pipeline to throttle it. Accordingly, the throttling pressure drop may be as high as 3 MPa or more. A good chill-down process of the pipeline system after the valve determines the stability of the engine hot-fire starting [26, 27]. In the previous study, a horizontal liquid oxygen pipeline contracted at the outlet of $D_i = 15$ mm was tested, the test pressure was varied in the range of 0.5~0.9 MPa, and the suggested correlations of T_{LFP} and q_{LFP}, T_{CHF}, and q_{CHF} were given [28]. The influence of two contracted forms, the orifice and injector, was further studied, and the phenomenon of cooling first in the middle of the horizontal pipeline was found, and the propagation law of the cooling head and the influence of the instable wave were analyzed [29]. The horizontal liquid oxygen pipeline ($D_i = 20$ mm) with the exit contracted was studied, and the pressure range was extended to 0.6-3.5 MPa, indicating that pressure has an important influence on LFP and CHF [30]. Further analysis of the horizontal pipeline δ_{LFP} and q_{CHF} was carried out to obtain the improved correlation equation [31]. In conclusion, the preliminary experiment studies the chilling process of the exit contracted liquid oxygen pipeline, including horizontal and vertical pipes, and the process indicates that the center of the pipe will be the first to form the quenching front and then spread to the sides of the pipe, and through a series of experiments, the new correlation of the boiling change point LFP and CHF is obtained.

However, there are still some problems, including the following: (1) L-shaped and Z-shaped test tubes are used, and there is a corner, which leads to the change of flow. For the QF (quenching front) at the entrance, the effect is not obvious in the horizontal L-shaped tube but has a certain effect in the vertical Z-shaped tube. It is believed that the corner has an impact on the effect of QF at the entrance. (2) The measuring points are still not dense enough, which leads to insufficient understanding of the cooling mechanism and some contradictions, mainly including the following: in the horizontal L-shaped pipe, the main QF is first formed in the middle of the pipe, while in the vertical Z-shaped pipe, the main QF is formed at the outlet and then propagated downward. Based on the previous study [28–31], further experimental research was carried out, including the inlet of this test which will be a directly used straight pipe, excluding the influence of the inlet effect. More wall temperature measuring points are arranged along the upper and lower sides of the outer wall of the test pipe section to reproduce the cooling and filling process more clearly and completely. A wide pressure range from 0.5 to 3.5 MPa was constructed in this round of the test, and the influence of throttling pressure on precooled filling will be further analyzed.

2. Experimental Methodology

2.1. Platform. Figure 1 gives the experimental platform applied in the present study, which is the LO_2 branch of a typical experiment platform for a cryogenic engine, different from that in the previous studies [28–31]. The experimental platform in the present study is with the same front-to-back relationship between the components, but the tank volume is larger to 2 m^3, which can be used for LO_2 with a larger flow rate and longer.

Upstream of the pipeline, the LO_2 in the storage tank is pressurized and transported by the nitrogen decompressed by the pressure reducer, and the pressurized nitrogen pressure is maintained at about 5 MPa after multiple experiments. The LO_2 storage tank is a cylindrical structure with vacuum jacket, and the pipeline is equipped with a pneumatic valve (main valve), cryogenic mass flow meter, Venturi tube, and necessary temperature and pressure sensors. The LO_2 flow is controlled by the venturi tube, which can keep the flow into the experiment section constant.

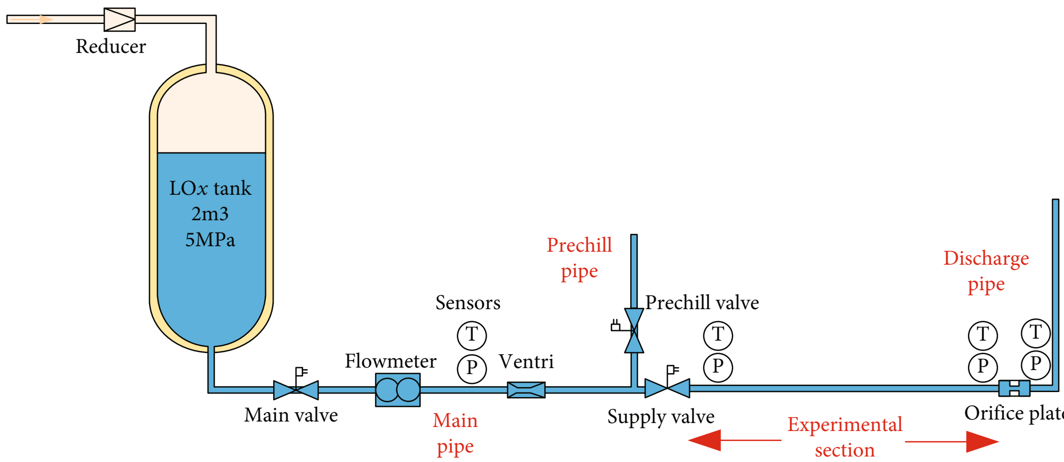

Figure 1: Experimental system of the present study.

Downstream line, including the precooling line and the experimental section could be shown in the figure. The precooling line is located in the front of the pneumatic valve (supply valve), and the experimental section is located behind the pneumatic valve (supply valve). During the experiment, the upstream line is cooled in advance by opening the precooling valve. Temperature and pressure sensors are also installed along the experimental section for the necessary data acquisition. A throttle orifice plate is installed at the outlet of the experimental section, and different experiments can provide different backpressure conditions by replacing the throttle orifice plate.

2.2. Experimental Section. Figure 2 gives the experimental section in detail. The size of the experimental section is 1200 mm in length; the inner diameter and wall thickness are 15 mm and 1.5 mm, respectively; and the material is stainless steel 316. Sensors for measuring fluid temperature and pressure are installed at the inlet and outlet of the experimental section. The temperature sensor is an insertion type, and the insertion depth of the measuring point is 5 mm. The experimental section is treated with polyurethane foam for thermal insulation, with a thickness of 20 mm, and the outer layer is also covered with aluminum foil tape to reduce the heat radiated from the outside.

14 T_o sensors (T-type thermocouples) were welded on the outer surface of the experimental section, and they were distributed over 7 sections as Figure 2(b) shows. Figure 2(b) gives the cross-section (vertical), where the 2 sensors were welded on the top and bottom of the pipe, respectively, which shows that for every section, 3 sensors were set up on the west, south, and east of the pipe in turn. All of the sensors are with the scan rate of 1000 Hz.

2.3. Experimental Measurement Method. Pressure, flow, and temperature are the main measurement parameters of the experiment. The pressure parameters are measured by piezoresistive sensors with a range of 0~10 MPa and a second-line output (4~20 mA) current signal. Fluid temperature measurement adopts thermal resistance temperature sensor (STT-100), the range is -200~50°C, and the temperature transmitter (STWB-TH-X100T) is a three-wire input and two-wire output (4~20 mA) current signal. The data scan rate used for these sensors is 1000 Hz.

The wall temperature was measured using a T-type thermocouple with a range of -200~50°C. LO_2 flow measurement adopts mass flowmeter, and the measurement range is 0~1 kg/s. The data scan rate used for these sensors is 100 Hz.

2.4. Experimental Procedure. Usually, a test is carried out according to the following process:

(1) *Filling of the LO_2 storage tank*. The maximum filling volume of the LO_2 storage tank is reserved for 20% of the gas space. When filling, the vent valve is fully opened and the filling flow is controlled so that the pressure in the storage tank is less than 0.5 MPa

(2) *Low-pressure precooling of the main pipeline*. Open the main valve and precooling valve, and use the pressure of the storage tank after filling to pressurize LO_2 to perform low-pressure precooling on the main pipeline. The precooling mass flow is 5-15 g/s, and the duration is usually more than 30 minutes. When there is continuous LO_2 flowing out of the outlet, and the mass flow and temperature are stable, it is considered that the low-pressure precooling meets the requirements

(3) *Pressurization of the LO_2 storage tank*. Before pressurizing the storage tank, the pressure in the storage tank should be less than 0.3 MPa. The storage tank is then pressurized by outputting nitrogen at a specific pressure by adjusting the pressure reducer

(4) *High-pressure chilling of the main pipeline*. The preparation process of pressurization and measurement and control sequence usually takes 3-5 min. The lack of flow of LO_2 in the pipeline will cause the temperature to rise to around -100°C. Therefore, in the test, the main pipeline was precooled at a high pressure

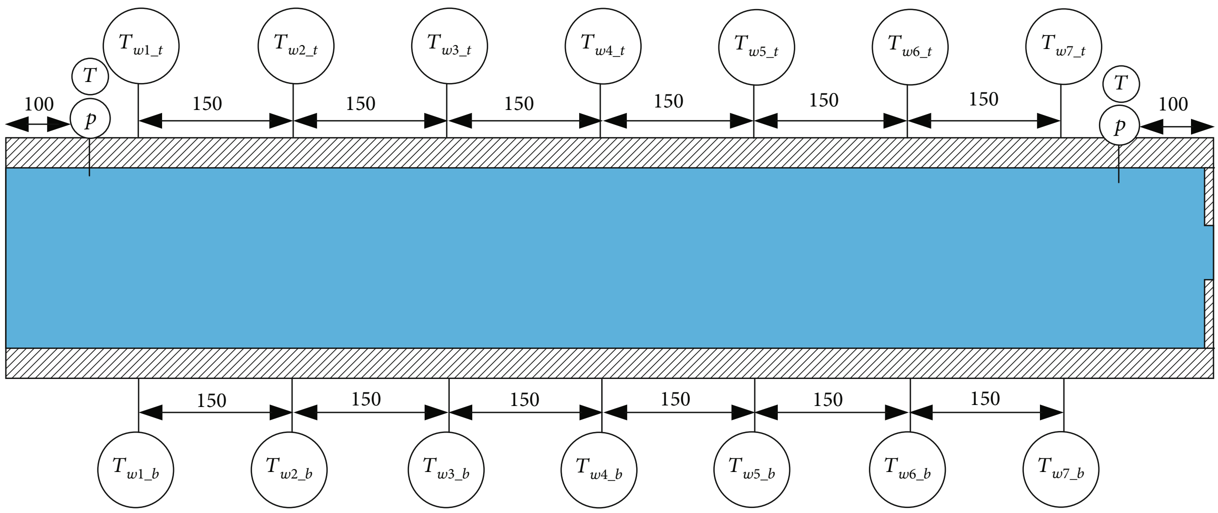

(a) Experimental section

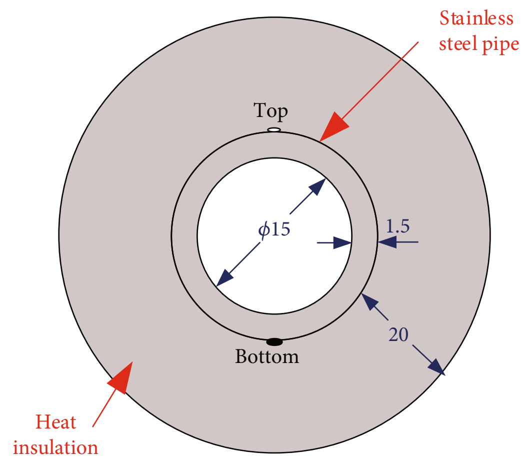

(b) Cross-section

FIGURE 2: Details on the experimental section, unit: mm.

for 40 s, and then, the LO_2 was switched from the precooling pipe to the experimental section

(5) *Chill-down test*. When the test section is precooled, a sufficient precooling test time should be ensured, and the LO_2 will be discharged into the atmosphere after passing through the experimental section

(6) *Rewarming of the experimental section*. The experimental section is blown out by an external nitrogen gas, and the pipe temperature is returned to normal temperature to wait for the next test

3. Experimental Results

3.1. Basic Results. Eight tests were carried out, and the test conditions and results are shown in Table 1. The tests were numbered according to the contracted orifice area A_{inj} from small to large, the corresponding contracted back pressure gradually increased from small to large, and the pressure in the pipe ranged from 0.57 to 3.49 MPa after stabilization.

These tests ranged from 0.549 to 0.564 kg/s after the liquid oxygen flow rate was stabilized, 332,150-364,457 after Re was stabilized, 107.5-108.9 K after the liquid oxygen outlet temperature (T_o) stabilized, and 7.1-108.9 K after the liquid oxygen outlet subcooling was stabilized. 36.9 K. During the test, when the supply valve is opened, when the liquid oxygen initially fills the pipeline, the pressure in the pipeline will appear as a pressure peak phenomenon, which will gradually increase with the reduction of the contracted area, and the range is 1.16-3.78 MPa.

3.2. Data Processing and Boiling Transition Points. Parameters in the pipe as well as T_o data were measured for all of the 8 tests. By processing the T_o data, T_i and q_i were obtained because most of the following discussions would be based on these 2 parameters. Here, T_i would be determined according to ref. [14], and q_i would be obtained by numerical methods introduced in the previous studies [28].

Based on T_i and q_i data, boiling curves could be drawn. In this way, the minimum q_i point and maximum q_i point would be determined. These two points are exactly the

Table 1: Experimental conditions and results.

Parameters	Exp. 1	Exp.2	Exp. 3	Exp. 4	Exp. 5	Exp. 6	Exp. 7	Exp. 8
A_{inj} (mm)	38.5	28.3	23.8	19.6	15.9	13.9	11.3	10.2
p_{ss} (MPa, end)	0.57	0.81	0.98	1.25	1.73	2.13	2.92	3.49
$\dot{m}$ (kg/s, start)	0.562	0.557	0.558	0.558	0.560	0.564	0.545	0.529
$\dot{m}$ (kg/s, end)	0.568	0.559	0.561	0.562	0.564	0.567	0.549	0.558
G (kg/(m^2•s), end)	3216	3166	3174	3180	3191	3206	3109	3159
Re (end)	336,904	364,457	358,647	356,428	352,989	346,567	332,150	342,916
T_p (K, end)	105.4	108.9	108.4	108.3	108.1	107.5	107.5	108.4
$T_{sat} - T_p$ (K, subcooling, end)	5.2	7.1	10.8	15.3	21.7	26.6	33.5	36.9
p_{peak} (MPa, start)	1.086	1.16	1.41	1.75	2.33	3.05	3.55	3.78

Table 2: Statistical t_{LFP}/t_{CHF} data (unit: s).

Position	Exp. 1	Exp. 2	Exp. 3	Exp. 4	Exp. 5	Exp. 6	Exp. 7	Exp. 8
0.15-T	4.4/6.7	3/4.8	2.8/4.2	2.2/3.6	1.6/2.8	1.4/2.3	1.3/2.1	1.8/2
0.15-B	4.9/6.1	4/5	3.5/4.2	2.2/3.7	1.9/2.9	1.4/2.3	2/2.1	1.7/2
0.30-T	16/18.9	11.6/13.6	7.1/9	4.7/7.5	3.1/5.4	2.5/4.1	3/3.3	3/3.3
0.30-B	15/17.6	12.6/13	7.1/8.9	6.6/7.3	4.2/5.4	2.6/4.1	3/3.5	1.8/3.3
0.45-T	23/26.1	13/16.9	8/10.7	8.2/9	6/6.6	1.5/5.2	2.5/4.2	1.9/4
0.45-B	23/28.6	9/16.4	9/11.2	8.2/9.8	0/6.8	0/5.2	0/3.4	0/3.1
0.60-T	17/23.1	15/19.4	8/12.8	5/10.4	1.9/7.4	1.3/5.7	1.1/4.7	1.2/4.4
0.60-B	23/24.6	15/16.7	10/11.1	8.8/9.3	1.9/7.1	1.3/5.5	1.1/4.6	1.2/4.3
0.75-T	23/28.7	16/20.9	12/14	6/11.2	1.7/8.2	1.6/6.2	1.4/5.1	1.3/4.7
0.75-B	20/23.4	15/16.3	10/10.9	9/9.4	2/7.4	1.4/5.9	1.2/5	1.3/4.5
0.90-T	24/31.1	15/22.4	12/15.1	6/12	2.2/9	1.4/7.2	1.3/5.7	1.3/5.3
0.90-B	24/27.8	17/19	11/12.7	6/10.5	1.4/8.4	1.4/6.6	1.2/5.4	1.6/5
1.05-T	2.9/5.3	4/5.8	2.3/4.5	2.1/3.6	2.1/4.1	1.4/3.8	1.3/3.6	1.4/3.4
1.05-B	3.1/9.5	4/9.7	2.3/6	2.2/5.2	2/5.7	1.6/5.1	1.4/4.9	1.5/4.3

so-called boiling transition points, which are denoted as LFP and CHF, respectively. As a result, basic data including p, T_i, q_i, and t on these boiling transition points could be obtained, which could be denoted as T_{LFP}, q_{LFP}, t_{LFP}, T_{CHF}, q_{CHF}, and t_{CHF}, etc.

Here, all of the t_{LFP} and t_{CHF} data could be collected and listed in Table 2, where t_{LFP} indicates the liquid rewetting (LFP) time from the chill-down start and t_{CHF} indicates the bubble separation time (CHF) from the chill-down start.

3.3. Uncertainty. The present study focuses on the comparison between experimental values and predicted values for T_{LFP}, q_{LFP}, T_{CHF}, and q_{CHF}. The experimental values depend mainly on the T_o measurement and physical properties as well as the geometric parameter of the pipe. On the other hand, as shown in the correlations, the predicted values depend mainly on the measured pressure and geometric parameter of the pipe. These factors are shown in Table 3.

Table 3: Summary of the uncertainties.

Parameters	Uncertainty
Fluid pressure (%)	0.5
Fluid temperature (K)	1
Outer wall temperature (K)	1
Pipe D_i and D_o (mm)	0.01
Mass flow rate (%)	1
T_o (K)	1
T_i (K)	2
q_i (%)	5

4. Chill-Down Process

In the previous study, the chill-down process has not been well defined. In the present study, it is necessary to denote that the chill-down process should be well described here. It is well known that the chill-down process starts from the time when the LO_2 first flows into the experimental section, and it finishes when the whole pipe (inner wall) gets to T_{sat}. However, in the present study, the nucleate boiling section will not be discussed. As a result, CHF is usually treated as the end of the chill-down process in the present study.

For a certain point with the T-type thermocouple on the outer surface of the wall, T_o could be measured and T_i could

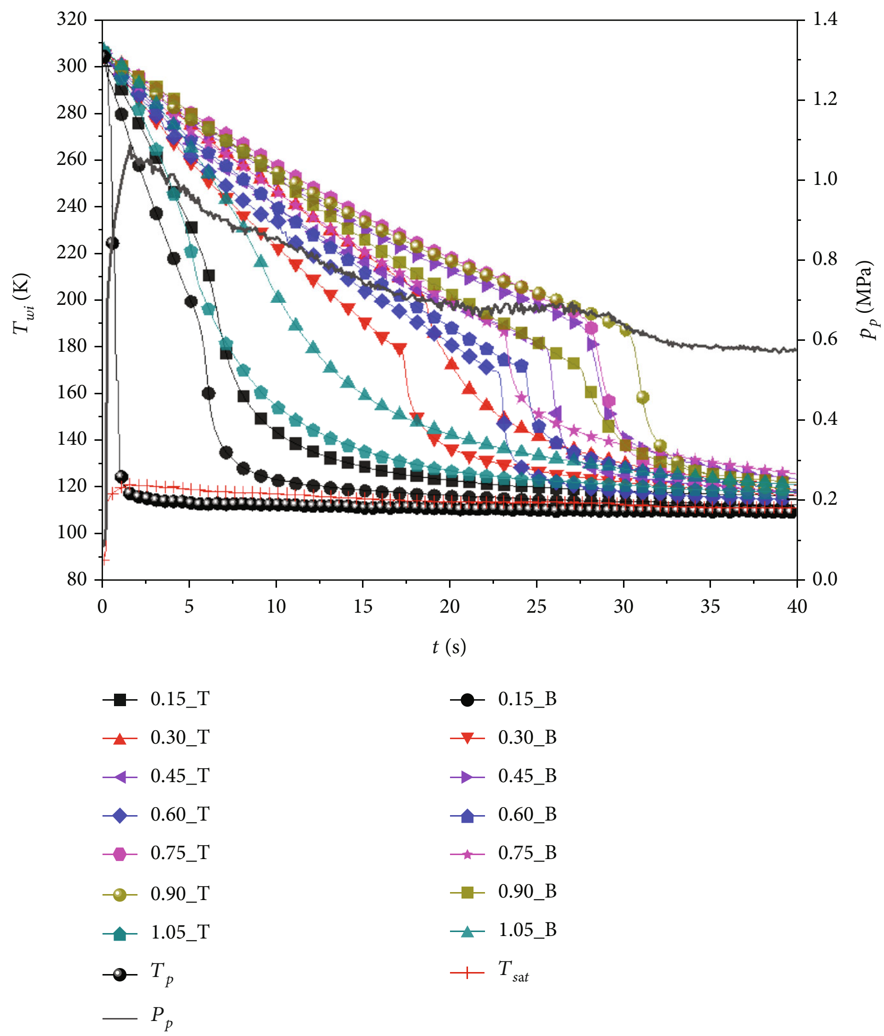

Figure 3: Data curves for Exp. 1 ($\dot{m} = 0.568$ kg/s, $p_{ss} = 0.57$ MPa).

be obtained. In this way, the basic history of the decreasing T_i as well as the q_i curve could be drawn, and the boiling transition points on this point could be obtained. For the whole pipe, based on the T_i data at various points, the historical T_i distribution could be drawn. However, this distribution is difficult to be drawn, and it could not play a significant role on analysis. In this way, for analysis, boiling transition points are extremely significant, by which the development of the flow pattern in the experimental pipe could be drawn.

As a result, in the present study, the chill-down process would be described by two items, the development of basic curves (all measured T_i and other parameters) and, more importantly, the development of the flow pattern in the experimental section. In most cases, the latter item is equal to the chill-down process.

As shown in Table 2, all of the eight tests could be classified into two groups roughly, the low-pressure condition, for Exp. 1~4, and the high-pressure condition, for Exp. 5~8. Apparently, the chill-down processes for these two groups are different from each other, according to the t_{LFP} and t_{CHF} data listed in Table 2. In the present section, the chill-down process for these two groups will be given in detail.

4.1. Chill-Down Process of Exp. 1. As the basic case, the chill-down process for Exp. 1 will be given in detail to show its basic manner.

4.1.1. Basic Curves Recorded. Figure 3 gives the data curves for Exp. 1. It shows that, as the LO_2 flows into the experimental section, because of the flash vaporization, pressure in the experimental section pipe increases sharply. On the other hand, temperature in the experimental section undergoes a sharp decrease. This is one of the primary characteristics of the cryogenic chill-down in the exit-contraction pipe for both the horizontal direction [30] and the vertical direction [31].

As shown in Figure 3, during the chill-down process, all of the wall temperature values show the typical manner of low-pressure chill-down. The T_i data curves show the obvious linear manner on the film boiling section, and a typical sharp decrease on the transition boiling and nucleate boiling section. As shown in the figure, T_i values on the $L_{se} = 0.15$ m

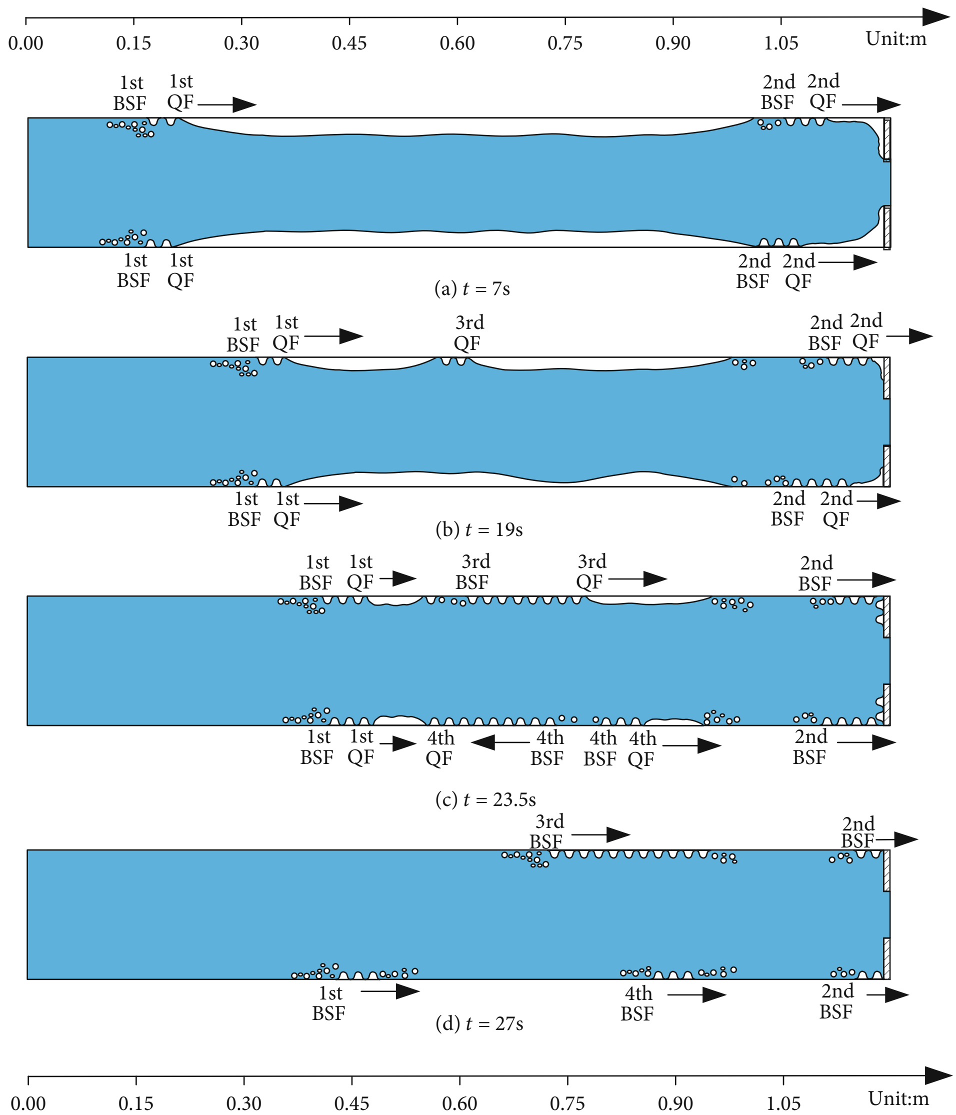

Figure 4: Flow patterns in the experimental section during the chill-down process for Exp. 1.

cross-section (0.15 m cross-section next for simplification) decrease at first with the lowest slope on the film boiling section, followed by 1.05 m, 0.3 m, and 0.6 in turn, and followed by the other sections including 0.45 m, 0.75 m, and 0.9 m, on which T_i values decrease by the similar slopes.

4.1.2. Development of Flow Pattern in the Experimental Section. As shown in Table 2, for Exp. 1, by considering the average values, LFP happens on the 1.05 m cross-section at first, followed by 0.15 m, 0.3 m, 0.6 m, 0.75 m, 0.45 m, and 0.9 m in turn. This sequence is very similar with the sequence of CHF happening, and the sequence of T_i slope discussed in Section 4.1.1.

Based on Table 2, the development of the flow pattern in the experimental section could be drawn as shown in Figure 4. For drawing these figures, the thickness of the vapor film for every sensor point instantaneously has been checked. This is the basic foundation to describe the chill-down process. As shown in the figures and table, for Exp. 1, as the LO_2 flows into the experimental section, which is the horizontal straight pipe, flash vaporization happens. The flow pattern in the whole pipe is immediately changed to a boiling film, by which the liquid core is surrounded by the vapor layer, which is in contact with the pipe wall.

Before 5.3 s, the inlet quenching front (QF), denoted as the 1st QF, has been formed and gets to the 0.15 m cross-section. Simultaneously, the exit QF (2nd QF) has been formed on the 1.05 m cross-section. A few seconds later, the inlet bubble separation front (the 1st BSF) is formed following the 1st QF and the 2nd BSF following the 2nd QF. All of these fronts propagate forward. As shown in Figure 4 and Table 2, it is evident that the 1st QF and the 1st BSF dominate the chill-down of the upper section of the experimental pipe, from the inlet to around 0.45 m cross-section. Similarly, the 2nd QF and the 2nd BSF dominate the chill-down of the end section of the experimental pipe, from around 1.05 m cross-section to the exit. After that, as shown in the figures and Table 2, the 3rd QF and the 4th QF have

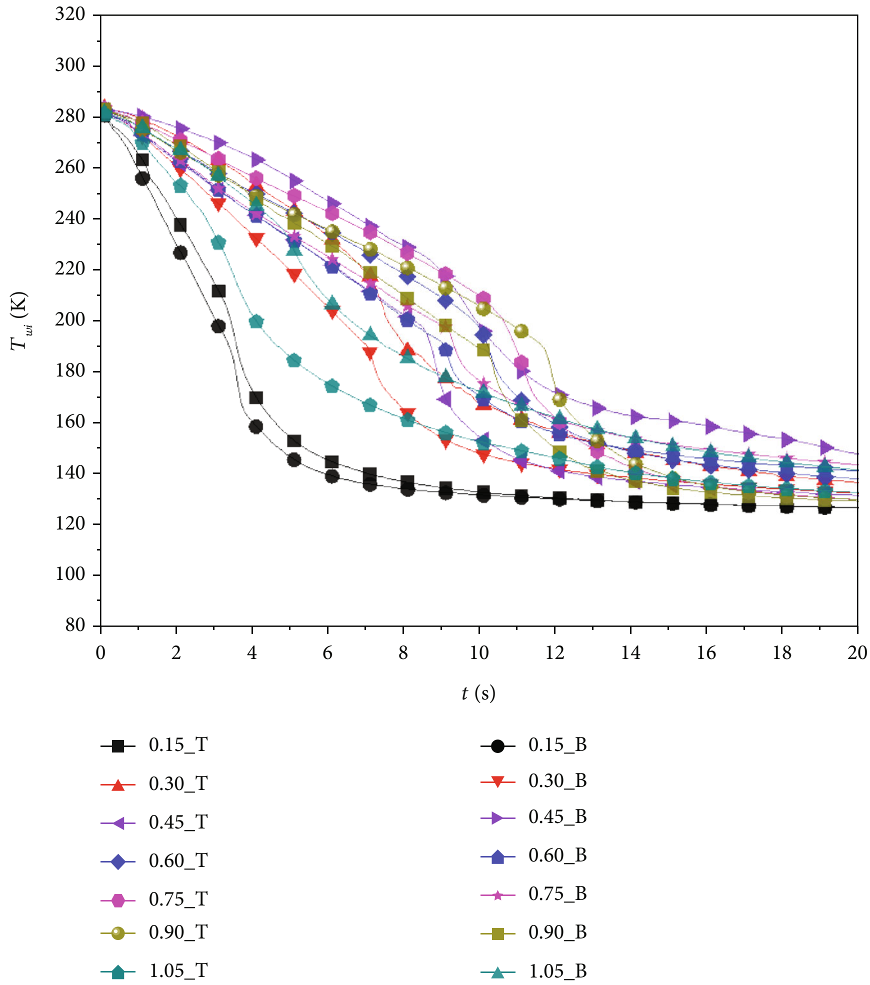

Figure 5: Data curves for Exp. 4 ($\dot{m} = 0.562$ kg/s, $p_{ss} = 1.25$ MPa).

been formed on 0.6-T and 0.75-B at 17 s and 20 s, respectively. After that, the 3rd BSF and the 4th BSF are formed on 0.6-T and 0.75-B at around 23.1 s and 23.4 s, respectively. The 3rd QF and BSF propagate forward, and the 4th QF and BSF propagate both forward and backward. As a result, it is evident that the chill-down of the section, from $L_{se} = 0.6$ m to $L_{se} = 0.9$ m is controlled by the 3rd and 4th fronts (QF and BSF).

4.2. Chill-Down Process for Low-Pressure Condition. Similarly, Figure 5 gives the basic T_i curves for Exp. 4, the $p_{ss} = 1.25$ MPa case. Comparison between Figures 3 and 5 shows that, for Exp. 4, during the chill-down process, most T_i curves show similar traits with those for Exp. 1. The primary difference is that the slopes of the linear section on the T_i curves in Figure 5 are much sharper than those in Figure 3. As a result, as shown in Table 2, t_{LFP} and t_{CHF} values for Exp. 4 are much lower than those for Exp. 1.

The flow patterns in the experimental pipe during the chill-down process for Exp. 4 can be shown in Figure 6. As shown in the figure, at 5 s, the 1st BSF gets to the 0.15 m cross-section, following the 1st QF at 0.3-T. Simultaneously, the 2nd BSF gets to the $L_{se} = 1.05$ m section (almost for 1.05-T), and the 3rd QF has been formed on 0.6-T. At 6 s, the section from 0.6-T to 0.9-T is rewetted because of the propagation of the 3rd QF, and the 4th QF has been formed on 0.9-B. At 8.2 s, the top surface of the experimental section has been rewetted completely because of the propagation of both the 1st QF and the 3rd QF. Furthermore, at 9 s, the bottom surface of the experimental section has been rewetted completely because of the propagation of both the 1st QF and the 4th QF. After that, it could be found that the CHF of the top surface of the experimental pipe is the propagation of the 1st BSF control, where the 3rd BSF has disappeared on the transitioned boiling section. On the other hand, similar to Exp. 1, the bubble separations of the bottom surface on the upper section (inlet to 0.45-T) and the section from 0.6-T to 0.9-T are controlled by the 1st BSF to the 4rd BSF, respectively.

Comparison shows that the so-called low-pressure condition includes Exp. 1~4, which is with both the similar manner of T_i curves and the development of the flow pattern in the experimental pipe.

4.3. Chill-Down Process for High-Pressure Condition. The T_i curves for Exp. 5 and Exp. 7 can be shown in Figures 7 and 8, respectively. As shown in the figures, the decrease of T_i curves is in the same manner, which is much different

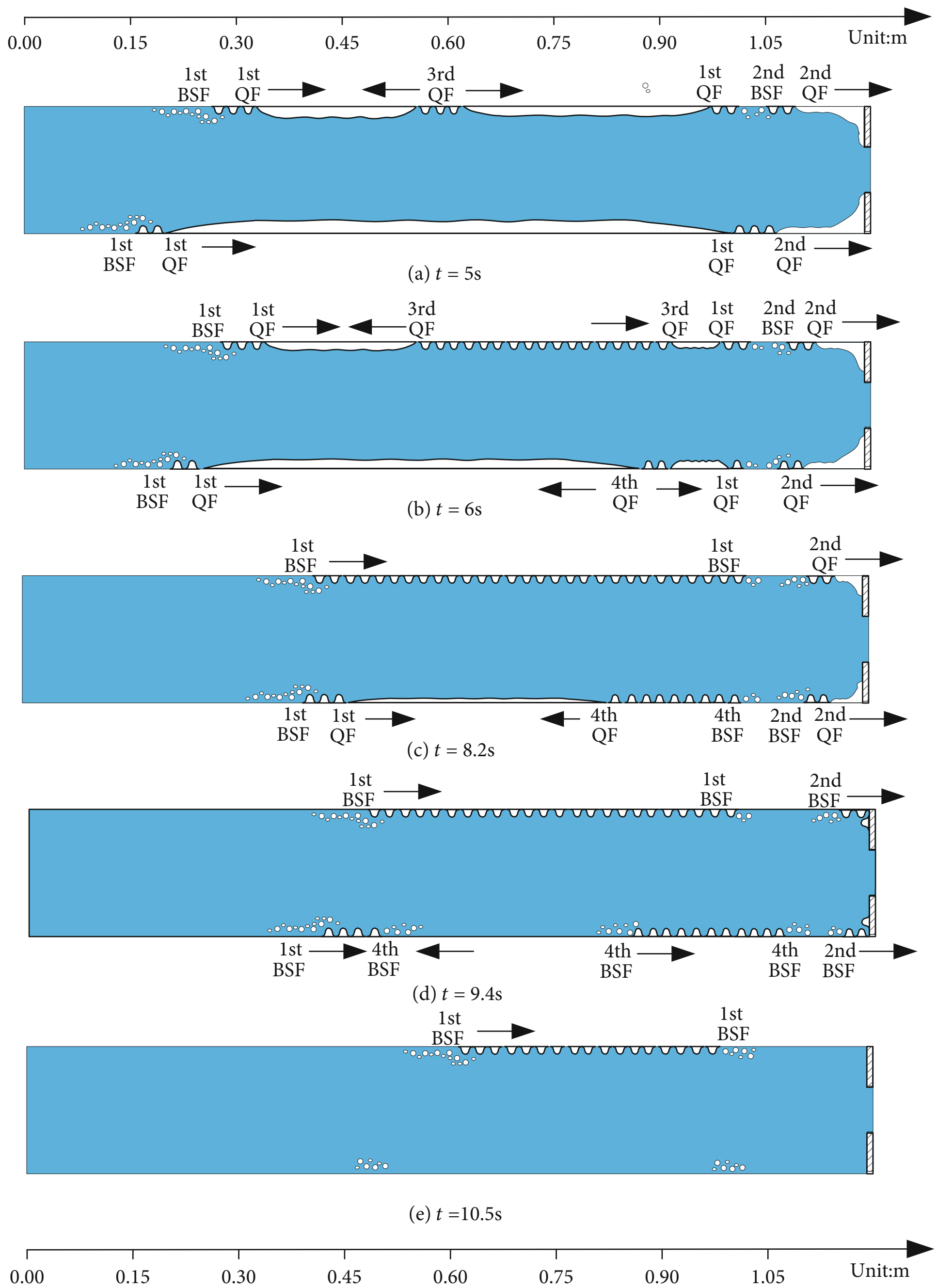

Figure 6: Flow patterns in the experimental section during the chill-down process for Exp. 4.

from that for the low-pressure condition. The T_i curves here are with the basic decreasing manner of linear-accelerated, followed by the gradual. As a result, the basic characteristics include that, at first, the linear section is extremely short, which indicates the shortened film boiling. On the other hand, the accelerated decrease section on the curve expands the long period, which indicates the relatively longer period of transition boiling.

Based on the figures and Table 2, the development of the flow pattern in the experimental section could be drawn as shown in Figure 9. Similarly, this figure could be also drawn for Exp. 7, which is similar with Exp. 5 and could not be drawn again. As shown in Figure 9(a), at around 2.2 s, the 1st QF gets to the 0.15 m cross-section, and on the other hand, the length from 0.6 m to 1.05 m of the experimental pipe has been rewetted almost simultaneously. The latter fact is obviously caused by the liquid fill-in. It could be supposed that two QFs would be formed here, the 2nd QF around the 1.05 m cross-section and the 3rd QF between the 0.45 m and 0.6 m cross-sections. After that, liquid rewetting happens on the 0.3 m and 0.45 m cross-sections in turn at 5.4 s and 6.6 s, respectively. This indicates that the liquid rewetting on the section from the inlet to 0.45 m is controlled by the propagation of the 1st QF, and the liquid rewetting on the section

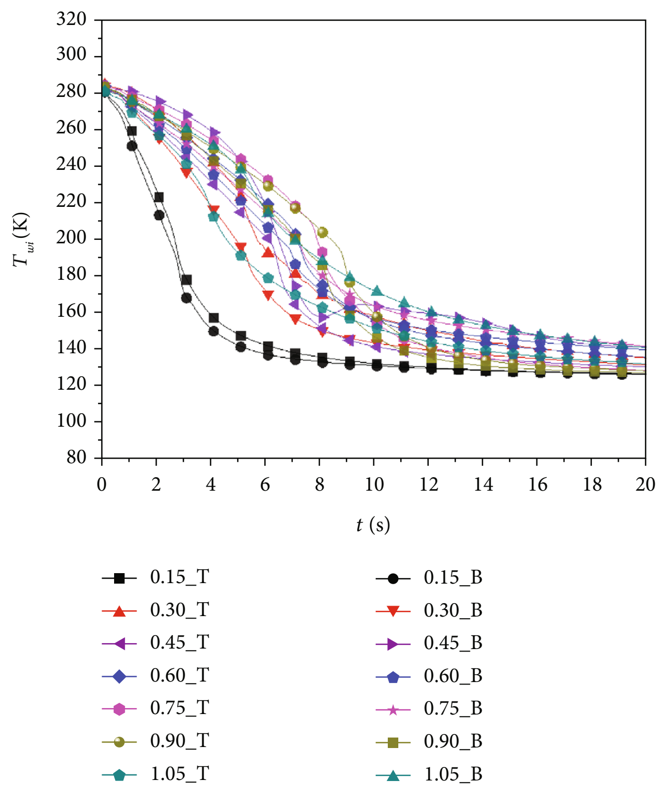

FIGURE 7: Data curves for Exp. 5 ($\dot{m} = 0.564$ kg/s, $p_{ss} = 1.73$ MPa).

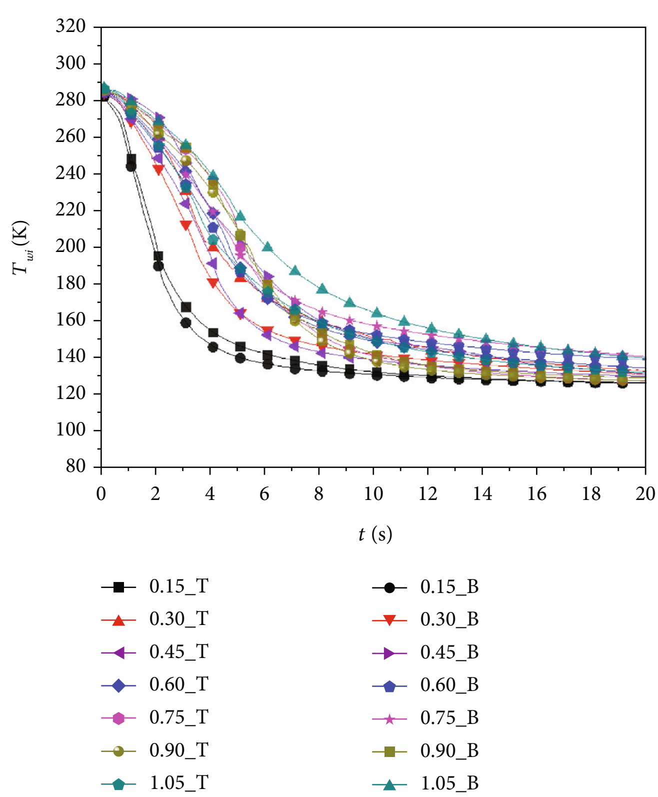

FIGURE 8: Data curves for Exp. 7 ($\dot{m} = 0.549$ kg/s, $p_{ss} = 2.92$ MPa).

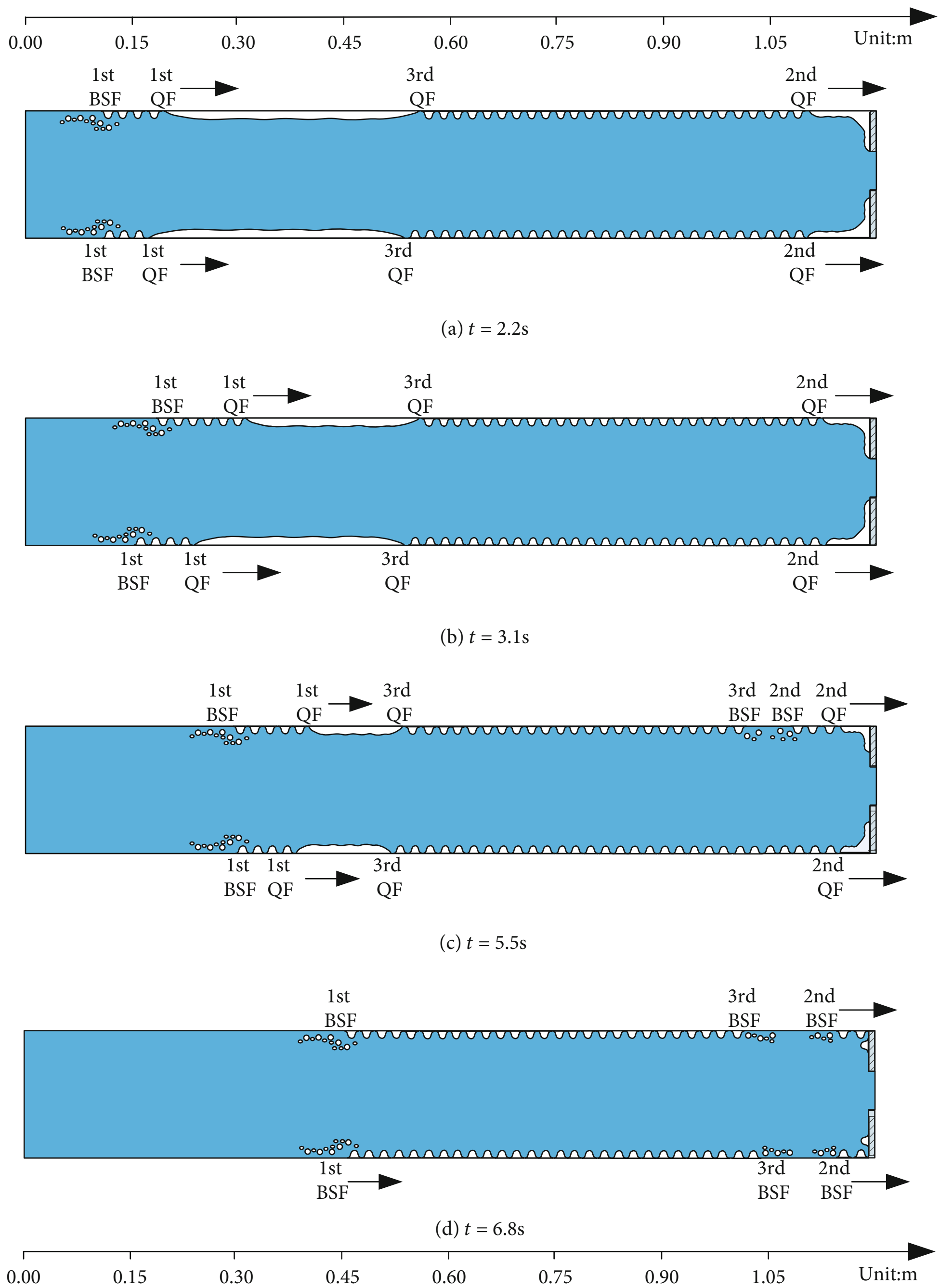

FIGURE 9: Flow patterns in the experimental section during the chill-down process for Exp. 5.

from 1.05 m to the exit is controlled by the propagation of the 2nd QF. However, the liquid rewetting on the section from 0.6 m to 1.05 m is controlled by the liquid fill-in, which is different from that for the low-pressure condition. With the increase of pressure, this section would be enhanced in length as shown in Table 2.

4.4. Chill-Down Process

4.4.1. Low-Pressure Condition. For the low-pressure condition (Exp. 1~4), as shown in Figures 3 and 5, the decrease of the T_i curve shows the linear-sharp-gradual manner, with the long linear section, corresponding to the relatively long period of film boiling. The increase of pressure reduces the linear section primarily, which reduces the t_{LFP} values as shown in Table 2. The experimental pipe could be divided into three sections based on the dominant factors as shown in Figure 10.

For both the pool boiling and the flow boiling, on the film boiling section, with the decrease of the wall temperature, the vapor thickness (δ) would undergo a decrease and the magnitude of the instable wave (M_w) would undergo an increase. Once these two parameters get to the same value, liquid rewetting happens here [32], which could be

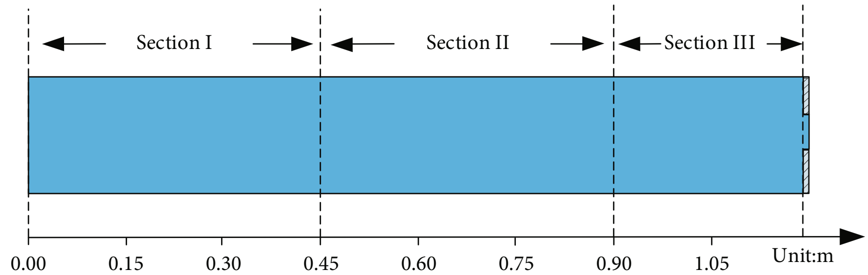

FIGURE 10: Sections divided in the experimental pipe.

denoted as LFP. This indicates two controlling factors of LFP, low δ or high M_w. The propagation of QF has been observed obviously in the studies on cryogenic chill-down in the transport pipe without exit-contraction [34].

Here, as shown in Figures 4 and 6, the liquid rewetting of the Section I and Section III would be always controlled by the 1st QF and the 2nd QF, respectively. On Section II, the extra QFs would be formed and propagated to control the liquid rewetting of this section during the chill-down process. For flow boiling, the area near QF has obviously the lowest δ and would get to LFP next, in which the development of flow is like the manner of "QF propagation." This could be denoted as the mechanism of QF propagation in the present study.

For the low-pressure condition (Exp. 1~4), with the development of chill-down, every QF concerned above would produce a BSF consistently, which would control the bubble separation on the corresponding section, and every BSF following QF has experienced adequately development. In this way, these BSFs would undergo the similar propagation with QF.

As shown in the ref. [14], bubble separation has been detected in cryogenic flow boiling. This point is denoted as CHF, or the bubble separation point, on which bubbles produced on the wall would flow into the main flow. This point is similar with LFP, which propagates downstream. In this way, BSF would be defined like QF. On BSF and its upstream, bubble separation would happen. Different from QF, the existence of BSF and its propagation are based on the fact that the heat flux that flows into the fluid is enough to vaporize the local liquid. This determined two characteristics of CHF or BSF. At first, it has to be following transition boiling. On the other hand, it is determined by the heat flux value (q_i), which has to be under adequately development before CHF.

4.4.2. High-Pressure Condition. For the high-pressure condition (Exp. 5~8), the decrease of the T_i curve shows the linear-accelerated-gradual manner as shown in Figures 7 and 8, with the long accelerated section, corresponding to the lengthened transition boiling section. It shows that the increase of pressure produces limited variations on both t_{LFP} and t_{CHF} as shown in Table 2. On the other hand, as shown in Figure 9, similar with the low-pressure condition, the liquid rewetting of Section I is always controlled by the 1st QF. However, the liquid rewetting of Section II and Section III is always suddenly obtained in a very short period, which indicates that it is controlled by the liquid fill-in during the chill-down process. This is controlled by another mechanism of LFP, high M_w, as mentioned above. With the increase of pressure, Section II would be prolonged.

With the LO_2 flows into the pipe, the vapor-liquid mixture could be blocked by the exit concentration. In this way, the mixture has to be accumulated on the second half of the pipe. For low pressure, this factor plays a weaker action. However, for high pressure, because of the low variations between the vapor phase and the liquid phase, the liquid is more likely to reach the inner wall here. On the other hand, h_{LFP} here is lower compared to the first half of the pipe, which indicates high δ_{LFP} and M_{LFP} here.

However, different from the low-pressure condition, for the high-pressure condition (Exp. 5~8), the bubble separation in Sections I and II is always controlled by the propagation of the 1st BSF, and the bubble separation in Section III is always controlled by the propagation of the 2nd BSF. CHF could not happen following the QFs on the second half of tube because both q_i (heat flux) and h_i (heat transfer coefficient) here have not experienced enough development. Or in other words, both q_i and h_i here are not high enough to get CHF. In this way, BSF propagates from the inlet to the outlet.

4.4.3. Classification. Basically, as discussed above, the decreasing manner of T_i curves and the development of the flow pattern in the experimental pipe for the low-pressure condition are much different from those for the high-pressure condition. This indicates that the process and mechanism of chill-down are different for these two groups.

As a result, based on the dominant factors of liquid rewetting, Table 4 can be listed.

5. Film Boiling Section and Leidenfrost Point

5.1. Leidenfrost Point

5.1.1. Basic Data. Figures 11 and 12 plot the data of ΔT_{LFP} and q_{LFP} versus p_{LFP}, respectively, which shows the basic effects of pressure on these parameters. As shown in the figures, all of the seven L_{se} cross-sections could be classified by a few methods based on the effects of p_{LFP} on ΔT_{LFP} or q_{LFP}. However, based on Equations (1) and (2), as well as the discussions in the previous studies [30, 31], δ_{LFP}, which indicates the thickness of the vapor film on LFP, is the primarily dominant parameter indicating the physical process. Sometimes, h_{LFP} would be discussed instead. In this way, all of the cross-sections would be classified into Class I and

Table 4: L_{se} range schematically.

Exp.	Section I	Section II	Section III
1	0~0.45 (2nd type)	0.6~0.9 (3rd type)	1.05~1.2 (2nd type)
2	0~0.45 (2nd type)	0.6~0.9 (3rd type)	1.05~1.2 (2nd type)
3	0~0.45 (2nd type)	0.6~0.9 (3rd type)	1.05~1.2 (2nd type)
4	0~0.45 (2nd type)	0.6~0.9 (3rd type)	1.05~1.2 (2nd type)
5	0~0.45 (2nd type)	0.6~0.9 (1st type)	1.05~1.2 (1st type)
6	0~0.3 (2nd type)	0.45~0.9 (1st type)	1.05~1.2 (1st type)
7	0~0.3 (2nd type)	0.45~0.9 (1st type)	1.05~1.2 (1st type)
8	0~0.3 (2nd type)	0.45~0.9 (1st type)	1.05~1.2 (1st type)

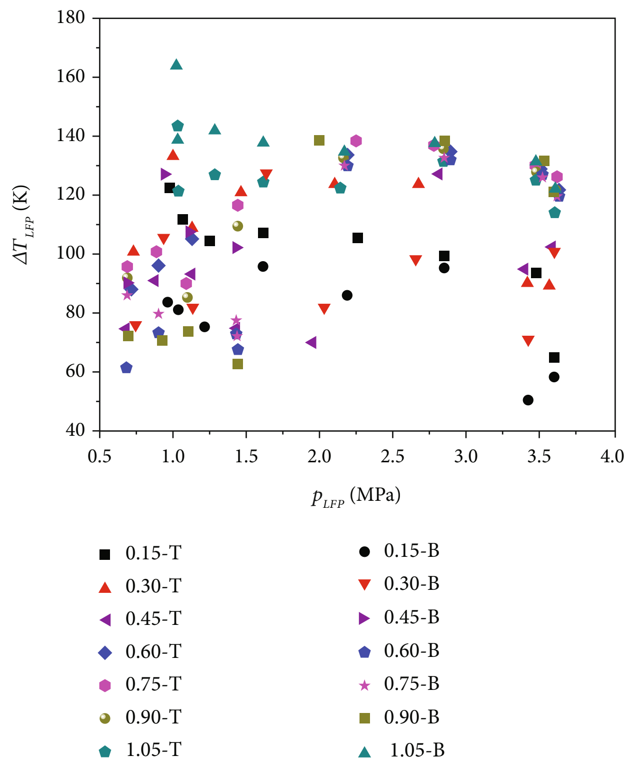

Figure 11: Experimental p_{LFP} versus ΔT_{LFP}.

Class II, according to the h_{LFP} data, which are consistent with the δ_{LFP} data.

$$h_{LFP} = \frac{q_{LFP}}{\Delta T_{LFP}}, \quad (1)$$

$$h_{LFP} = \frac{k_v}{\delta_{LFP}}. \quad (2)$$

5.1.2. Cross-Sections in Class I. Class I includes both 0.15 m and 0.3 m cross-sections. Parameters h_{LFP} and δ_{LFP} could be plotted versus p_{LFP} as shown in Figures 13 and 14, respectively. On these cross-sections, with the increase of pressure, h_{LFP} undergoes the increasing manner and δ_{LFP} undergoes the overall decreasing manner, which is the basic characteristic of this class. This basic characteristic is mainly caused by the fact that these sections are near to the inlet, the QF formation area. This is similar to the other cases in the previous studies, the so-called "heat transfer control" manner, $L_{se} = 0.75$ m for the L-shaped horizontal experimental section [30] and $L_{se} = 1$ m for the Z-shaped vertical experimental section [30]. The primary difference between the present study and the previous studies is the pressure range. In the present study, the p_{ss} tested ranges from 0.57 to 3.55 MPa. However, in the previous studies, the tested p_{ss} values were below 2 MPa [30, 31].

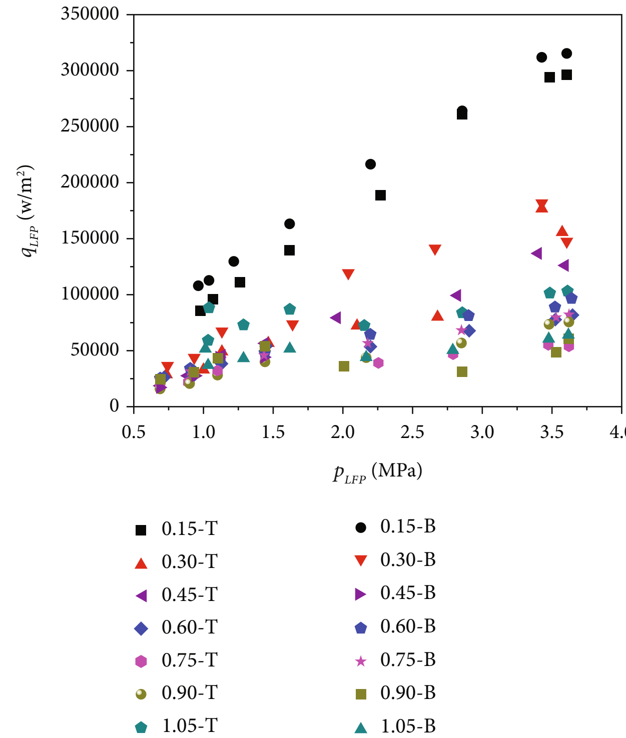

Figure 12: Experimental p_{LFP} versus q_{LFP}.

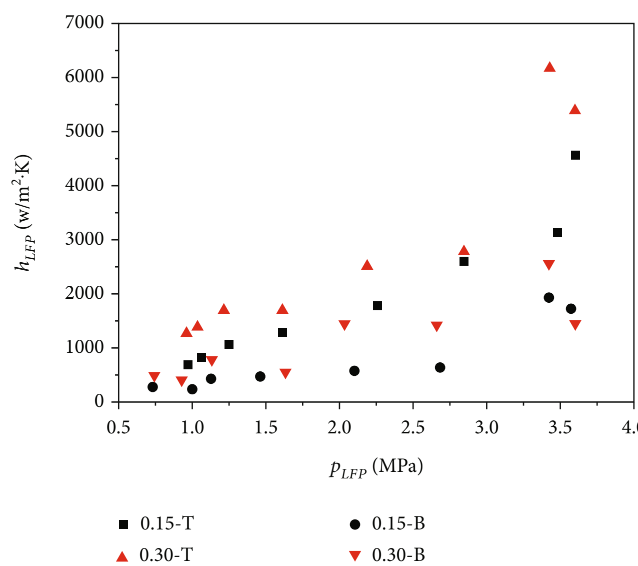

Figure 13: h_{LFP} versus p_{LFP} for class I.

As shown in Figures 13 and 14, the increase of pressure produces continuously increasing h_{LFP}, due to the decreasing

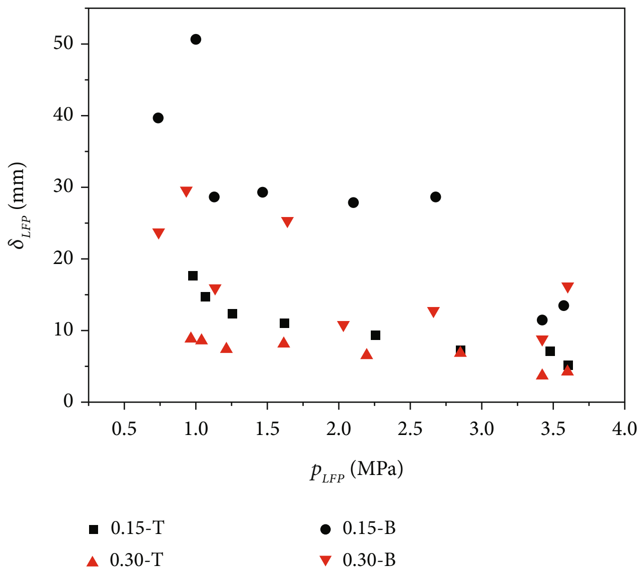

Figure 14: δ_{LFP} versus p_{LFP} for class I.

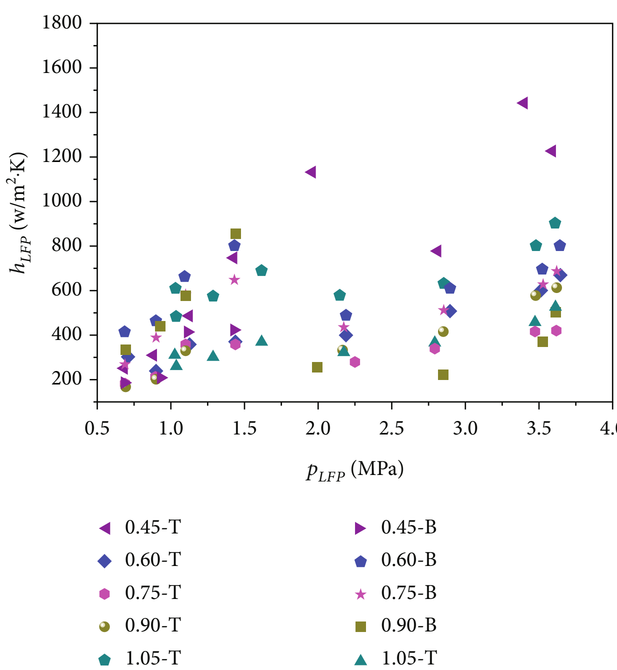

Figure 15: h_{LFP} versus p_{LFP} for class II.

δ_{LFP} and increasing k_v as shown in Equation (2). This is based on the fact that the increase of pressure would produce lower MLFP (magnitude of instable wave) in such a wide pressure range. Another fact is that throughout the pressure range in the present study, the basic mechanism of liquid rewetting has not been converted for Class I, which is always controlled by the propagation of the inlet QF as discussed in Section 4.4.

5.1.3. Cross-Sections in Class II. Class II includes all of the other cross-sections. Parameters h_{LFP} and δ_{LFP} could be plotted versus p_{LFP} as shown in Figures 15 and 16. With the increase of pressure, h_{LFP} shows the obvious "N" shape,

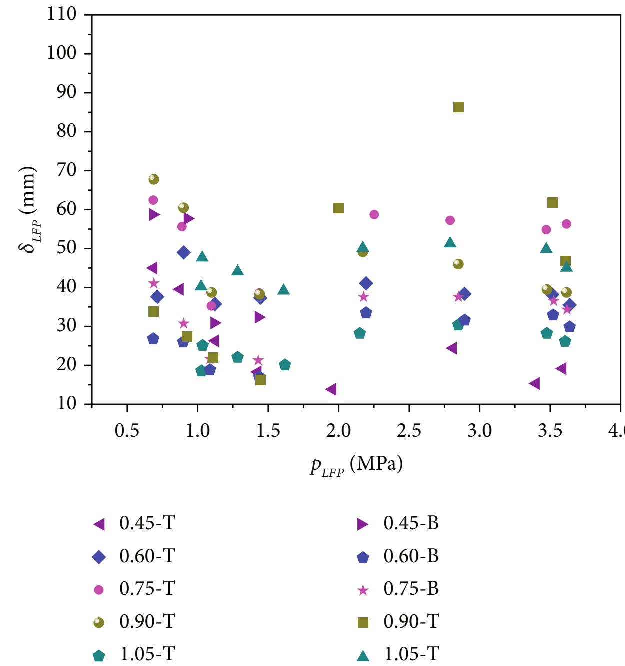

Figure 16: δ_{LFP} versus p_{LFP} for class II.

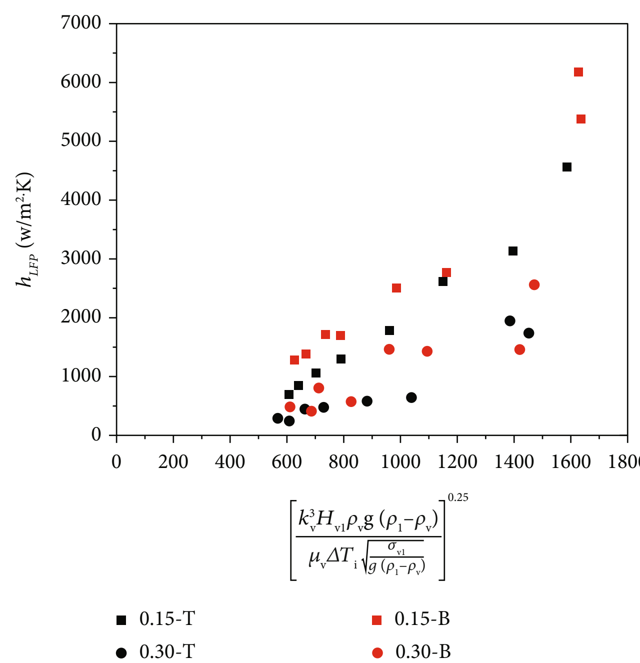

Figure 17: h_{LFP} versus $[k_v^3 H_{vl}\rho_v g(\rho_l-\rho_v)/\mu_v \Delta T_i \sqrt{\sigma_{vl}/g(\rho_l-\rho_v)}]^{0.25}$ for cross-sections in Class I.

and δ_{LFP} shows the inverted "N" shape. This is the primary characteristic here. For Class II, h_{LFP} shows the increasing manner from Exp. 1 to 4. After that, it undergoes a certain drop from Exp. 4 to 5 (from Exp. 5 to 6 for 0.45-T), followed by another section increase from Exp. 5 to Exp. 8. Likewise, the distribution of δ_{LFP} shows the consistent inverted manner, which undergoes a certain enhancement from Exp. 4 to 5 as shown in Figure 16.

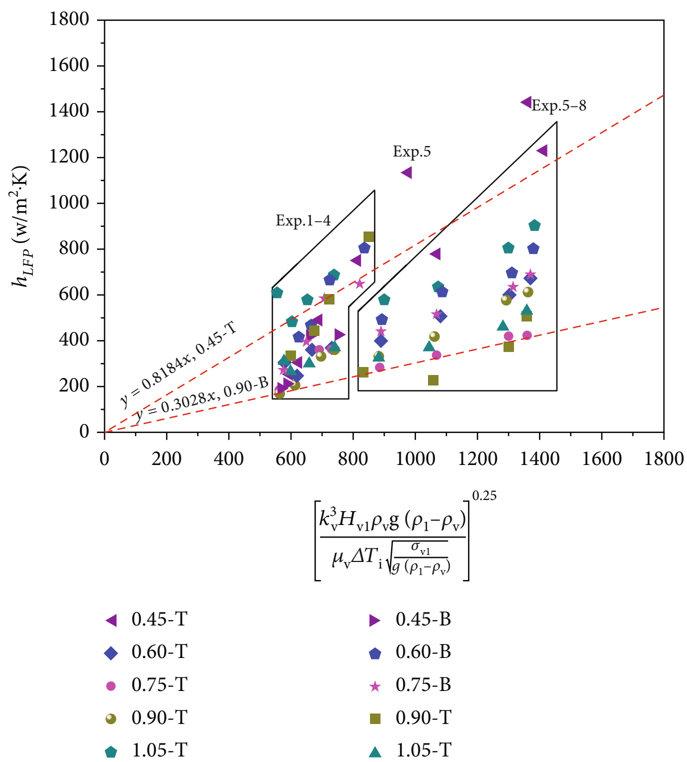

FIGURE 18: h_{LFP} versus $[k_v^3 H_{vl}\rho_v g(\rho_l-\rho_v)/\mu_v \Delta T_i\sqrt{\sigma_{vl}/g(\rho_l-\rho_v)}]^{0.25}$ for cross-sections in Class II.

This phenomenon is primarily caused by the conversion of the liquid rewetting mechanism as discussed in Section 4.4. On these cross-sections, liquid rewetting is controlled by the QF propagation for low-pressure cases (Exp. 1~4, or Type I discussed in Section 4.2). However, on the high-pressure cases (Exp. 5~8, or Type II discussed in Section 4.3), liquid rewetting is controlled by the local QF produced by liquid fill-in. This conversion on the liquid rewetting mechanism from Exp. 4 to Exp. 5 produces a certain increase of δ_{LFP}. This indicates that for these sections, M_{LFP} (magnitude of the instable wave, equal to δ_{LFP}) produced by the propagated QF is greater than that produced by the produced QF locally.

Obviously, this conversion is produced by the increase of p_{ss} from 1.25 to 1.73 MPa or the increase of p_{LFP} from 1.5 to 2.1 MPa. With the increase of pressure in this range, on the cross-sections from around 0.45 m to 1.05 m, the factor of liquid fill-in overcomes the factor of QF propagation as the dominant factor, which produces the dramatic reductions on t_{LFP} as shown in Table 2. In particular, for the L_{se} = 1.05 m section, the dominant factor of liquid rewetting converts from the propagation of the exit QF to the local QF produced by the liquid fill-in.

5.2. Correlation on Heat Transfer Coefficient. In the previous study, h_{LFP} could be well correlated by Equation (3), where C_2 could be various constants for various points [31].

$$h_{LFP} = C_2\left[\frac{k_v^3 H_{vl}\rho_v g(\rho_l-\rho_v)}{\mu_v \Delta T_i\sqrt{\sigma_{vl}/g(\rho_l-\rho_v)}}\right]^{0.25}. \quad (3)$$

In the present study, we try to correlate h_{LFP} via Equation (3) for cross-sections of 0.15 m and 0.3 m as shown in Figure 17 and for other cross-sections as shown in Figure 18, where some exception points have been removed. As shown in the figures, for the points (Sections II and III for Exp. 5~8, as shown in Table 4) where liquid rewetting is controlled by the local QF produced by liquid fill-in, h_{LFP} could be well correlated via Equation (3), in which various C_2 can be shown in Table 5. It shows that reliable predictions could be obtained for these points.

However, for the other conditions, where liquid rewetting is controlled by the propagation of QF, the slopes of h_{LFP} increase are obviously greater than those predicted by Equation (3). In this way, for these conditions, we will try to prove a new correlation approach, and Equation (4) could be set up. By data fitting as shown in Figure 19, C_1 and C_2 could be determined for these points and listed in Table 5. As shown in the figure and table, for the points on 0.15 m, 0.3 m, and 1.05 m, C_1 has been determined to be 0.4326, and for other points, C_1 has been obtained to be 0.6926. It shows that h_{LFP} could be well predicted in this way.

$$h_{LFP} = C_2\left[\frac{k_v^3 H_{vl}\rho_v g(\rho_l-\rho_v)}{\mu_v \Delta T_i\sqrt{\sigma_{vl}/g(\rho_l-\rho_v)}}\right]^{C_1}. \quad (4)$$

5.3. Discussions

5.3.1. Correlation Approaches. As shown in Table 4, data points could be classified into three types, which could be correlated by three equations, respectively. From the 1st type

Table 5: C_1 and C_2 values and deviations.

Position	Range	C_1 in Eq. (4)	C_2 in Eq. (4)	Error (%)	Range	C_2 in Eq. (3)	Error (%)
0.15-T	Exp. 1~8	0.4326	0.012187	-8.1~14.6			
0.3-T	Exp. 1~8	0.4326	0.005214	-26.8~34.6			
0.45-T	Exp. 1~5	0.6926	5.92×10^{-6}	-11.5~14.5	Exp. 6~8	0.8184	-5.9~12.2
0.6-T	Exp. 1~4	0.6926	4.72×10^{-6}	-11.9~8.7	Exp. 5~8	0.4712	-3.6~4
0.75-T	Exp. 1~4	0.6926	4.38×10^{-6}	-10.8~6.0	Exp. 5~8	0.3174	-1.6~1.7
0.9-T	Exp. 1~4	0.6926	4.03×10^{-6}	-7.8~6.3	Exp. 5~8	0.4269	-5.2~13.2
1.05-T	Exp. 1~4	0.4326	0.007574	-2.4~1.8	Exp. 5~8	0.6289	-3.5~6.2
0.15-B	Exp. 1~8	0.4326	0.016669	-10.9~21.1			
0.3-B	Exp. 1~8	0.4326	0.008878	-18.9~21.9			
0.45-B	Exp. 1~4	0.6926	4.94×10^{-6}	-23~9.6	—	—	—
0.6-B	Exp. 1~4	0.6926	7.23×10^{-6}	-9.4~11.9	Exp. 5~8	0.5577	-4.2~5.1
0.75-B	Exp. 1~4	0.6926	6.3×10^{-6}	-14.2~14.9	Exp. 5~8	0.4894	-2.8~2.1
0.9-B	Exp. 1~4	0.6926	6.6×10^{-6}	-5.4~3.7	Exp. 5~8	0.3028	-18.3~43.8
1.05-B	Exp. 1~4	0.4326	0.0040	-1.9~1.4	Exp. 5~8	0.3686	-4.7~4.1

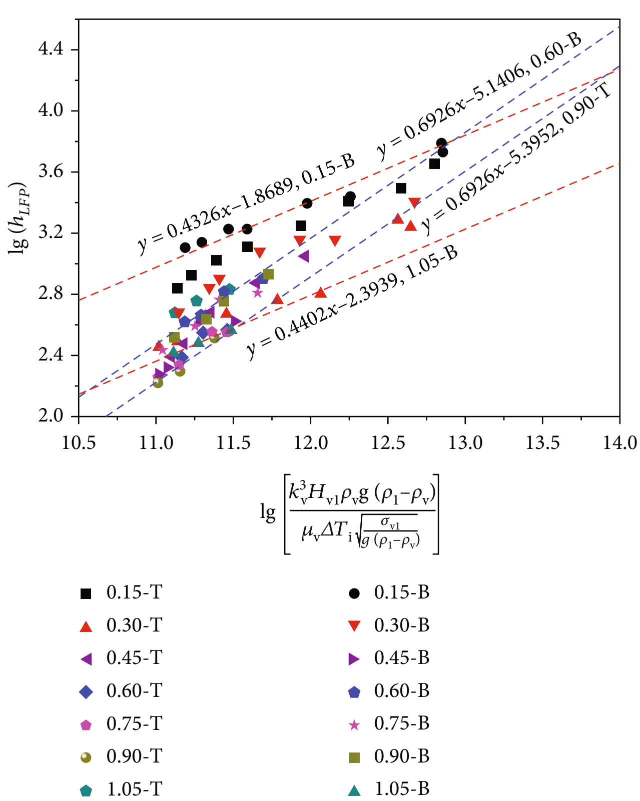

Figure 19: Correlation on h_{LFP}.

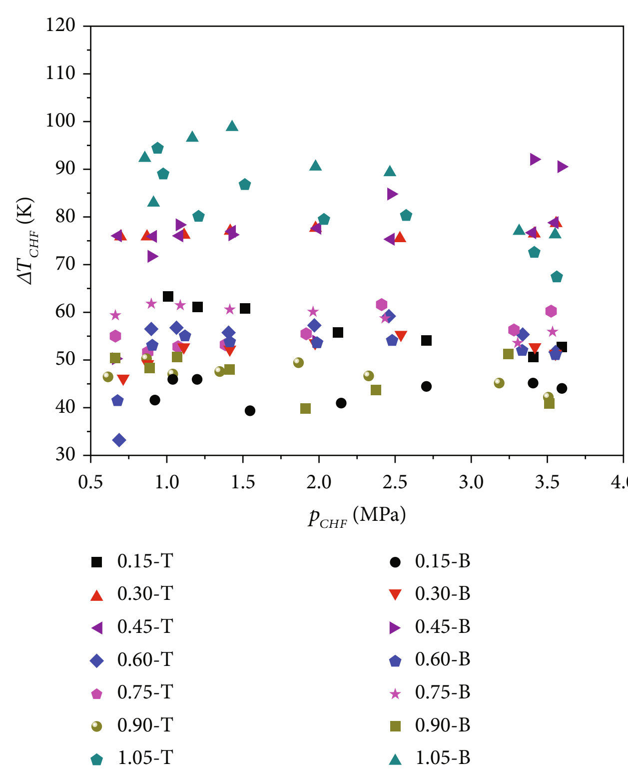

Figure 20: Experimental ΔT_{CHF} versus p_{CHF}.

to the 3rd type, the effect of pressure plays an increasing role on the increase of h_{LFP}.

For the 1st type, for Section II, Exp. 5~8 and Section III, Exp. 5~8 as shown in Table 4, h_{LFP} could be correlated via Equation (3). This equation is proven from film boiling originally [32]. The order of C_2 in Equation (3) as shown in Table 5 is similar with 0.425 in surface film boiling [32]. Here, because of liquid fill-in at high pressure, liquid rewetting would be obtained simultaneously on the various cross-sections in Sections II and III. This indicates that this sort of liquid rewetting is similar in mechanism with film boiling.

For the 2nd type, for Section I, Exp. 1~8 and Section III, Exp. 1~4 as shown in Table 4, h_{LFP} could be correlated via Equation (5). Here, cross-sections 0.15, 0.3, and 1.05 are similar with each other, on which the liquid rewetting is controlled by the propagation of the end (inlet or exit) QF. Both

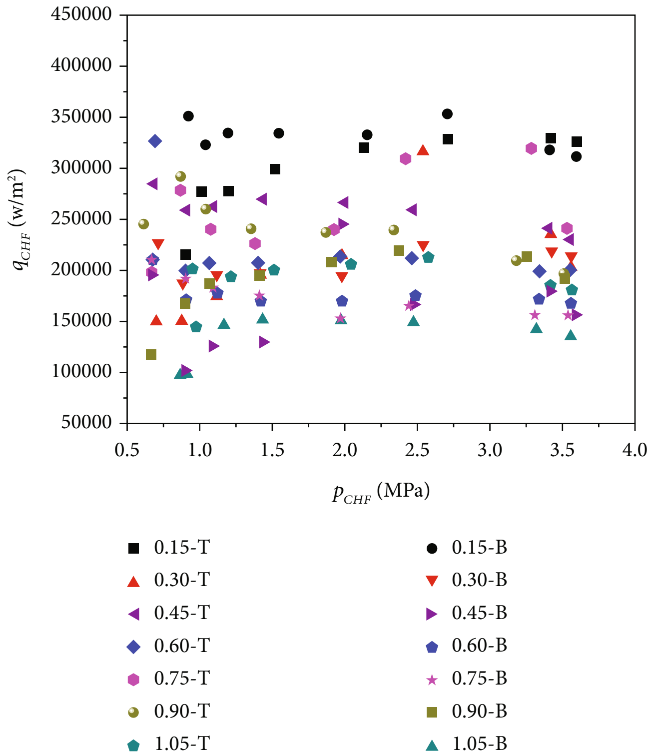

FIGURE 21: Experimental q_{CHF} versus p_{CHF}.

the inlet QF and the exit QF could be detected in the previous study [31].

$$h_{\mathrm{LFP}} = C_2 \left[\frac{k_{\mathrm{v}}^3 H_{\mathrm{vl}} \rho_{\mathrm{v}} g (\rho_{\mathrm{l}} - \rho_{\mathrm{v}})}{\mu_{\mathrm{v}} \Delta T_{\mathrm{i}} \sqrt{\sigma_{\mathrm{vl}} / g (\rho_{\mathrm{l}} - \rho_{\mathrm{v}})}} \right]^{0.4326}. \quad (5)$$

For the 3rd type, for Section II, Exp. 1~4 in Table 4, h_{LFP} could be correlated via Equation (6). Here, on these cross-sections, the liquid rewetting is controlled by the propagation of the 3rd QF and the 4th QF, which could be called the central QFs. They are always formed in Section II independently.

$$h_{\mathrm{LFP}} = C_2 \left[\frac{k_{\mathrm{v}}^3 H_{\mathrm{vl}} \rho_{\mathrm{v}} g (\rho_{\mathrm{l}} - \rho_{\mathrm{v}})}{\mu_{\mathrm{v}} \Delta T_{\mathrm{i}} \sqrt{\sigma_{\mathrm{vl}} / g (\rho_{\mathrm{l}} - \rho_{\mathrm{v}})}} \right]^{0.6926}. \quad (6)$$

5.3.2. The Effect of Factors. As shown in Figures 13 and 15, except the cross-sections of 0.45 m and 1.05 m, h_{LFP} values at the bottom are always higher than those at the top as shown in the figures. This indicates the effect of gravity, in which, for most cases, δ_{LFP} at the bottom is thinner than that at the top.

Basically, along the direction of QF propagation, h_{LFP} would undergo a decreasing manner. As shown in the figure, comparison shows that because of the propagation of the 1st QF, h_{LFP} values show the decreasing manner from cross-sections 0.15 m to 0.3 m. On the other hand, because of the

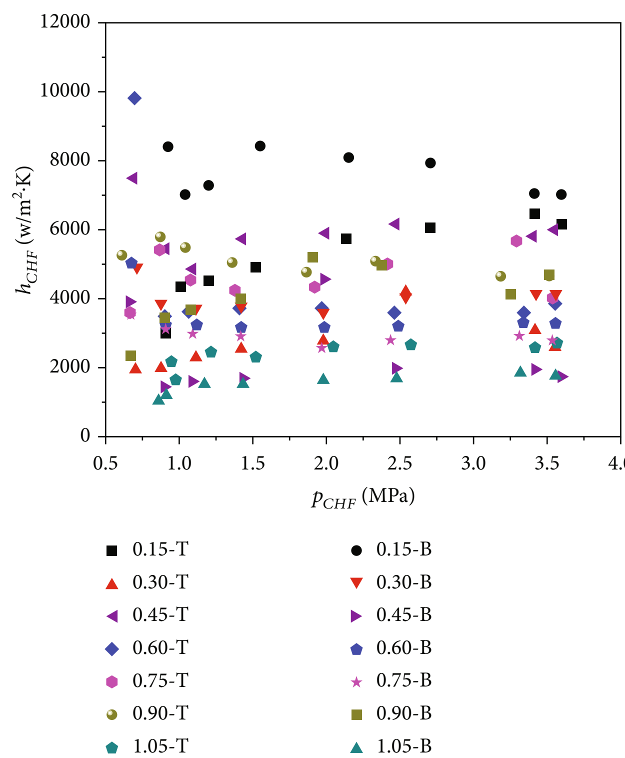

FIGURE 22: Experimental h_{CHF} versus p_{CHF}.

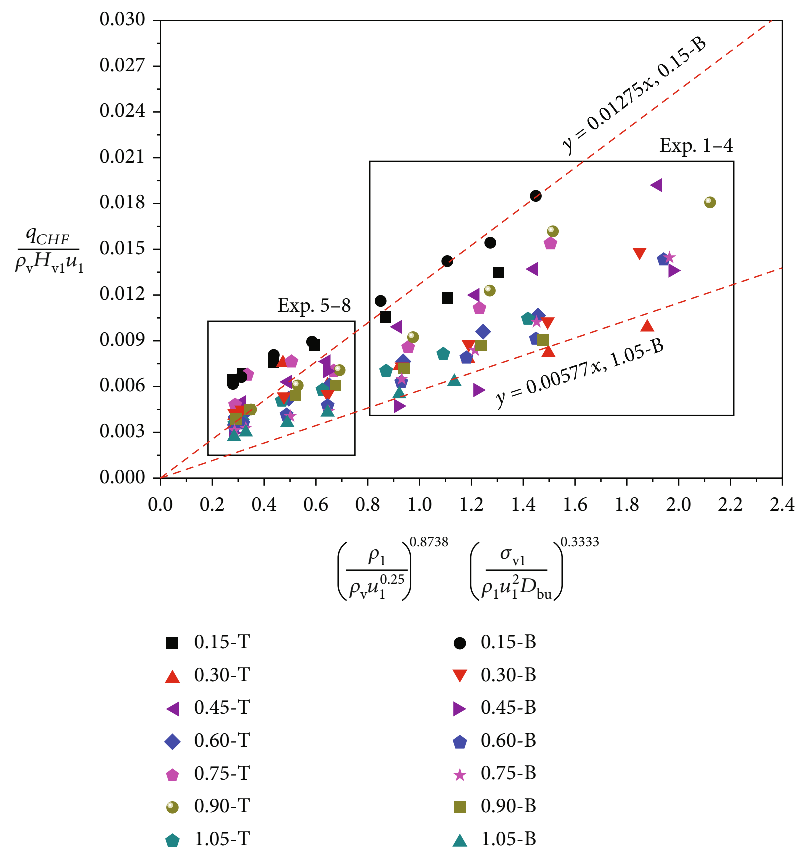

FIGURE 23: Correlation on q_{CHF} by Equation (7).

propagation of the 3rd and the 4th QF, h_{LFP} values show the decreasing manner from cross-sections 0.6 m to 0.75 m.

6. Critical Heat Flux

6.1. Basic Data. Figures 20–22 plot the data of ΔT_{CHF}, q_{CHF}, and h_{CHF} versus p_{CHF}, respectively, which show the basic effects of pressure on these parameters. As shown in the figures, with the increase of pressure, all of the parameters ΔT_{CHF}, q_{CHF}, and h_{CHF} show the overall constant manner, except for a few special points.

For LFP, the liquid rewetting is caused by the magnitude of the instable wave increase to the thickness of the vapor film. As a result, h_{LFP} is the dominant parameter compared to q_{LFP} and ΔT_{LFP}. However, for CHF, the basic bubble separation mechanism is that q_{CHF} supplied to the fluid could be completely used to supply the latent heat of the bubble vapor flow out from the inner wall. This indicates that q_{CHF} is the dominant parameter compared to h_{CHF} and ΔT_{CHF}. As shown in Figure 21, the effect of p_{CHF} on q_{CHF} in the present study is similar with that in the previous studies [30, 31].

Basically, with the increase of pressure, q_{CHF} values undergo the constant-decreasing manner for most of the points. The exceptions include the following.

(1) From Exp. 1 to Exp. 2, the variations that q_{CHF} values undergo do not show an obvious manner on some points. This is because Exp. 1 has been performed on different seasons from other tests. In this way, from the point of view of correlation, some points would be excluded

(2) For 0.9-B and 1.05-B, with the increase of pressure, q_{CHF} values undergo the constant-decreasing manner, which is different from the primary manner

(3) For 0.3-T, 0.45-B and 0.75-T, some q_{CHF} values are extremely higher than the others

6.2. Correlations on the Critical Heat Flux. In the previous studies, Equation (7) has been proven to predict q_{CHF} in the exit-contracted pipe. This equation has been validated for both horizontal and vertical pipes below around 2 MPa [30, 31]. In the present study, q_{CHF} data could be plotted versus the right side of Equation (7) as shown in Figure 23, where a few exception data have been excluded. As shown in the figure, it is evident that Equation (7) could give reliable predictions on the q_{CHF} data for the low-pressure condition (Exp 1~4) as discussed above, where the C_3 data is listed in Table 6. However, this equation could not give reliable predictions on q_{CHF} for the high-pressure condition as shown in Figure 23. As shown

Table 6: C_3 values and deviations.

Point	C_3 in Eq. (7)	Deviation (%)	C_3 in Eq. (9)	Deviation (%)
0.15-T	0.01086	-10.83~4.5	0.05248	-5.55~5.52
0.30-T	0.00586	-25.35~10.87	0.03551	-8.53~5.62
0.45-T	0.00997	-7.84~4.39	0.03996	-4.12~2.82
0.60-T	0.00765	-7.36~4.55	0.03300	-2.1~1.61
0.75-T	0.00962	-6.05~6.92	0.03917	-3.4~3.6
0.90-T	0.00937	-12.33-9.72	0.03494	-6.75~6
1.05-T	0.00755	-7.15~2.38	0.03148	-3.12~3.16
0.15-B	0.01275	-6.74~4.95	0.05278	-2.53~2.71
0.30-B	0.00759	-5.43~10.11	0.03415	-5.79~12.49
0.45-B	0.00616	-10.7~29.71	0.02968	-22.82~16.21
0.60-B	0.00694	-6.02~9.52	0.02735	-3.08~4.57
0.75-B	0.0072	-2.64~3.63	0.02523	-3.86~4.57
0.90-B	0.00677	-12.65~9.87	0.03334	-2.88~2.72
1.05-B	0.00577	-4.7~3.22	0.02312	-1.83~1.26

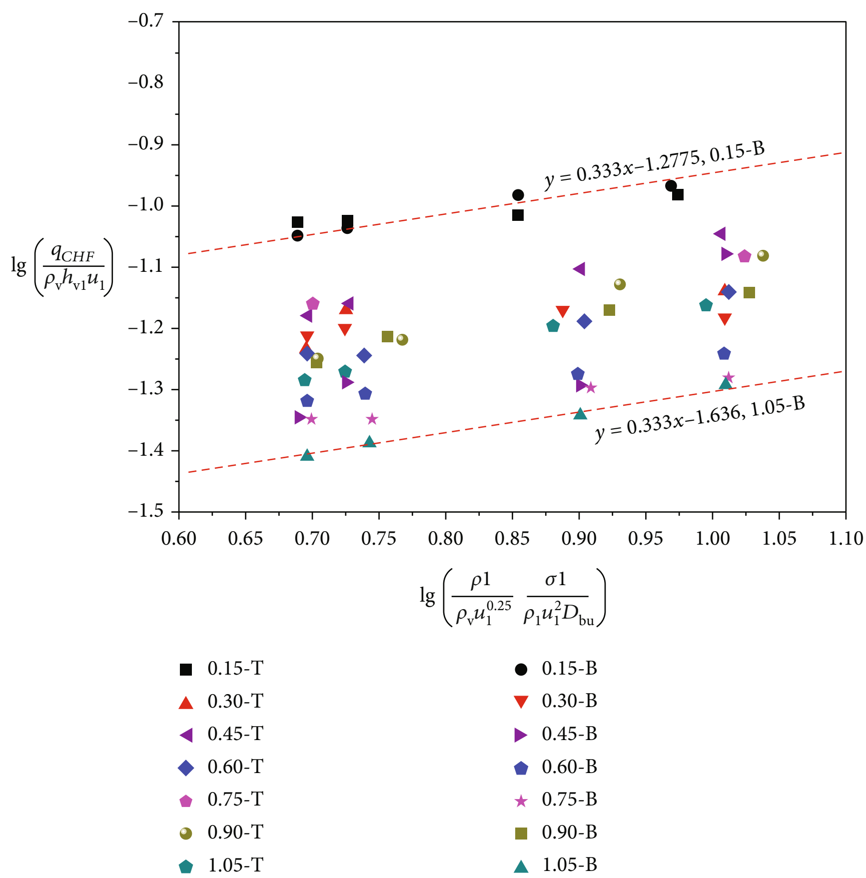

Figure 24: High-pressure condition.

in the figure, for the high-pressure condition, the slope is lower.

$$\frac{q_{\mathrm{CHF}}}{\rho_v H_{vl} u_l} = C_3 \left(\frac{\rho_l}{\rho_v u_l^{0.25}}\right)^{0.8738} \left(\frac{\sigma_{vl}}{\rho_l u_l^2 D_{bu}}\right)^{0.3333}. \quad (7)$$

In this way, the basic correlation on q_{CHF} proven in reference [30] should be given in Equation (8). For the high-pressure condition, the experimental q_{CHF} data could be correlated by Equation (8) as shown in Figure 24. Here, the exponent m has been correlated to be 0.333, and C_3 is correlated and listed in Table 6.

It shows that by Equation (9), q_{CHF} could be well predicted.

$$\frac{q_{\mathrm{CHF}}}{\rho_{\mathrm{v}} h_{\mathrm{vl}} u_{\mathrm{l}}}\left(\frac{\sigma_{\mathrm{l}}}{\rho_{\mathrm{l}} u_{\mathrm{l}}^{2} D_{\mathrm{bu}}}\right)^{-1/3} = C_{3}\left(\frac{\rho_{\mathrm{l}}}{\rho_{\mathrm{v}} u_{\mathrm{l}}^{0.25}}\right)^{m}, \quad (8)$$

$$\frac{q_{\mathrm{CHF}}}{\rho_{\mathrm{v}} h_{\mathrm{vl}} u_{\mathrm{l}}} = C_{3}\left(\frac{\rho_{\mathrm{l}}}{\rho_{\mathrm{v}} u_{\mathrm{l}}^{0.25}}\right)^{0.333}\left(\frac{\sigma_{\mathrm{l}}}{\rho_{\mathrm{l}} u_{\mathrm{l}}^{2} D_{\mathrm{bu}}}\right)^{0.333}. \quad (9)$$

6.3. Discussions

6.3.1. Correlation Approaches. Compared to h_{LFP}, the correlation of q_{CHF} is based on the pressure range. For the low-pressure condition (Exp. 1~4), q_{CHF} could be correlated by Equation (7), and for the high-pressure condition (Exp. 5~8), q_{CHF} could be correlated by Equation (9), where the constant is listed in Table 6.

6.3.2. The Effect of Factors. As shown in Figure 21, basically, q_{CHF} values on the top surface are higher than those on the bottom surface. This is because bubble separation is more difficult on the top surface [33].

Based on the discussions above, basically, along the propagation of BSF, q_{CHF} would undergo continuous decrease. As shown in Figure 21, on the low-pressure condition, q_{CHF} values undergo the obvious decreasing manner from cross-sections 0.15 m to 0.3 m. After that, on the low-pressure condition, q_{CHF} values undergo continuous increase on two sections, from 0.6-T to 0.9-T and from 0.45-B to 0.75-B. This is probably caused by the BSFs followed by the 3rd and 4th QFs.

For the high-pressure condition, q_{CHF} values undergo continuous decrease from 0.15-B to 0.9-T primarily, which is also consistent with the propagation of BSF as discussed in Section 4.4.

7. Conclusion

In the present study, the LO_2 chill-down in a straight horizontal pipe was studied experimentally. Compared to the previous studies, the effect of the entrance corner was excluded, and more dense wall temperature sensors along the pipe have been set. In this way, the chill-down process, as well as the development of the flow pattern, has been drawn for every test. As a result, the mechanism of the LO_2 chill-down would be obtained for various pressure sections. Based on the transition points obtained, h_{LFP} and q_{CHF} could be correlated by new approaches, where the basic parameter combinations are the same with the previous studies. Conclusions show that the correlation equations are dependent to the chill-down mechanisms. Detailed conclusions could be listed as follows.

(1) On the low-pressure condition (Exp. 1~4, $p_{\mathrm{ss}} \leq 1.25$ MPa), the decrease of T_{i} curves shows the linear-sharp-gradual manner, with the long linear (film boiling) section. In addition, the liquid rewettings in Sections I and III are controlled by the propagation of the end QF, and the liquid rewetting in Section II is controlled by the propagation of the QF produced in the present section. Every QF would produce the corresponding BSF, which controls the bubble separation in the present section

(2) On the high-pressure condition (Exp. 5~8, $p_{\mathrm{ss}} \geq 1.25$ MPa), the decrease of the T_{i} curve shows the linear-accelerated-gradual manner, with the long accelerated (transition boiling) section. In addition, the liquid rewetting in Section I is controlled by the propagation of the inlet QF, and the liquid rewetting in other sections is controlled by the sudden fill-in of the liquid. Bubble separation in Section III is obviously caused by the exit BSF following the exit QF. However, in other sections, it is controlled more likely by the propagation of the inlet BSF following the inlet QF

(3) For Sections II and III, Exp. 5~8 as shown in Table 4, h_{LFP} could be correlated by Equation (3), which is consistent to the liquid rewetting mechanism, which is a sudden liquid fill-in. For Section I, Exp. 1~8 and Section III, Exp. 1~4 in Table 4, h_{LFP} could be correlated by Equation (5), which corresponds to the related controlling factor, the propagation of the end QFs. For other cases, h_{LFP} could be predicted by Equation (6), which is consistent with the controlling factor, the propagation of the central QFs

(4) Based on the previous correlation format [30], Equations (7) and (9) are proven to predict q_{CHF} for the low-pressure condition and high-pressure condition, respectively. Both the present q_{CHF} data and constant C_3 for the low-pressure condition show obvious consistency with those from the L-shaped horizontal pipe and Z-shaped vertical pipe

Nomenclature

A: Area, m^2
B: Parameter combination in correlations
C: Constant in correlations
c: Specific heat, $J \cdot kg^{-1} \cdot K^{-1}$
D: Diameter, m
E: Parameter combination in correlations
G: Mass flux in the experimental section, $kg \cdot m^{-2} \cdot s^{-1}$
g: Gravity acceleration, $m \cdot s^{-2}$
H: Latent heat or enthalpy, $J \cdot kg^{-1}$
h: Heat transfer coefficient, $W \cdot m^{-2} \cdot K^{-1}$
k: Heat conductivity, $W \cdot m^{-1} \cdot K^{-1}$, or constant in k_{FZ}
L: Distance, m
$\dot{m}$: Mass flow rate, $kg \cdot s^{-1}$
N: Number of data
p: Pressure, Pa
Pr: Prandtl number, $c_{\mathrm{p}} \cdot \mu \cdot k^{-1}$
q: Heat flux, $W \cdot m^{-2}$
Re: Reynolds number, $D_{\mathrm{i}} G \cdot \mu_{\mathrm{l}}^{-1}$
T: Temperature, K

t: Time, s
u: Velocity, m/s
V: Variables mainly represent T_{LFP}, q_{LFP}, T_{CHF}, and q_{CHF} data.

Subscripts

bu: The bubble
CHF: Critical heat flux point
cr: Critical properties
exp: Experimental data
FZ: Forster-Zuber parameter
FB: Film boiling
i: The inner wall of the pipe
inj: Injector on the pipe exit
LFP: Inner wall data of the Leidenfrost point
l: Liquid phase
NB: Nuclear boiling
o: The outer wall of the pipe
p: Fluid in the experimental section or constant pressure in c_{p}
peak: Value of the pressure peak
pre: Predicted data by correlations
s: The solid material
sat: Saturation condition
se: From main valve to outer wall temperature sensors
si: Saturation parameter on inner wall temperature
ss: Steady-state condition, the chill-down finishes
v: Vapor phase
vl: From vapor phase to liquid phase.

Greek Symbols

μ: Viscosity, Pa·s
ρ: Density, kg·m^{-3}
σ: Surface tension, N·m^{-1}
δ: Thickness of film, m.

Data Availability

Data have been uploaded via "supplemental files" with the manuscript file.

Conflicts of Interest

The authors declare that they have no conflicts of interest.

Acknowledgments

This study was funded by the National Natural Science Foundation of China (grant number T2221002).

Supplementary Materials

In the "Supplementary files" section, a file named "Data_A," including the LFP and CHF data in the format of a table, has been uploaded with the manuscript. All the related data on boiling transition points, both LFP and CHF, are listed in Tables 1 and 2, respectively, of the file. In Table 1, p_{LFP} (pressure on LFP), q_{LFP} (inner wall heat flux on LFP), t_{LFP} (time spent from LFP to chill-down starting), T_{LFP} (inner wall temperature on LFP), T_{sat} (saturation temperature corresponding to p_{LFP}), and h_{LFP} (inner wall heat transfer coefficient on LFP) are listed for all of the 14 points for Exp. 1~8. In this way, both vapor properties and liquid properties could be determined for these points from Exp. 1~8. In Table 2, p_{CHF} (pressure on CHF), q_{CHF} (inner wall heat flux on CHF), t_{CHF} (time spent from CHF to chill-down starting), T_{CHF} (inner wall temperature on CHF), T_{sat} (saturation temperature corresponding to p_{CHF}), and h_{CHF} (inner wall heat transfer coefficient on CHF) are listed for all of the 14 points for Exp. 1~8. In this way, both vapor properties and liquid properties could be determined for these points from Exp. 1~8. *(Supplementary Materials)*

References

[1] D. Conte, D. Budzyn, H. Burgoyne et al., "Innovative Mars Global International Exploration (IMaGInE) mission-first place winning paper," in *AIAA SPACE*, p. 5596, Long Beach, California, 2016.

[2] E. A. Hurlbert, H. Ueno, L. Alexander et al., "International space exploration coordination group assessment of technology gaps for LOX/methane propulsion systems for the global exploration roadmap," in *AIAA SPACE 2016*, p. 5280, Long Beach, California, September 2016.

[3] P. Cui, Q. Li, P. Cheng, and L. Chen, "System scheme design for LOX/LCH4 variable thrust liquid rocket engines using motor pump," *Acta Astronautica*, vol. 171, pp. 139–150, 2020.

[4] L. Yin, E. Jiaqiang, J. Ding, and Y. Li, "An experimental study on the spray characteristics of splash platelet injector," *Acta Astronautica*, vol. 181, pp. 377–383, 2021.

[5] J. Hartwig, S. Darr, and A. Asencio, "Assessment of existing two phase heat transfer coefficient and critical heat flux correlations for cryogenic flow boiling in pipe quenching experiments," *International Journal of Heat and Mass Transfer*, vol. 93, pp. 441–463, 2016.

[6] J. N. Chung, J. Dong, H. Wang, S. R. Darr, and J. W. Hartwig, "Enhancement of convective quenching heat transfer by coated tubes and intermittent cryogenic pulse flows," *International Journal of Heat and Mass Transfer*, vol. 141, pp. 256–264, 2019.

[7] J. N. Chung, S. R. Darr, J. Dong, H. Wang, and J. W. Hartwig, "Heat transfer enhancement in cryogenic quenching process," *International Journal of Thermal Sciences*, vol. 147, article 106117, 2020.

[8] L. Zhou, T. Pan, H. Wang, D. Liu, and P. Wang, "Rapid air expulsion through an orifice in a vertical water pipe," *Journal of Hydraulic Research*, vol. 57, no. 3, pp. 307–317, 2019.

[9] L. Zhou, H. Wang, B. Karney, D. Liu, P. Wang, and S. Guo, "Dynamic behavior of entrapped air pocket in a water filling pipeline," *Journal of Hydraulic Engineering*, vol. 144, no. 8, p. 04018045, 2018.

[10] L. Jin, C. Park, H. Cho, C. Lee, and S. Jeong, "Experimental investigation on chill-down process of cryogenic flow line," *Cryogenics*, vol. 79, pp. 96–105, 2016.

[11] L. Jin, H. Cho, C. Lee, and S. Jeong, "Experimental research and numerical simulation on cryogenic line chill-down process," *Cryogenics*, vol. 89, pp. 42–52, 2018.

[12] L. Jin, H. Cho, and S. Jeong, "Experimental investigation on line chill-down process by liquid argon," *Cryogenics*, vol. 97, pp. 31–39, 2019.

[13] L. Jin, J. Lee, and S. Jeong, "Investigation on heat transfer in line chill-down process with various cryogenic fluids," *International Journal of Heat and Mass Transfer*, vol. 150, article 119204, 2020.

[14] H. Hu, J. N. Chung, and S. H. Amber, "An experimental study on flow patterns and heat transfer characteristics during cryogenic chilldown in a vertical pipe," *Cryogenics*, vol. 52, no. 4-6, pp. 268–277, 2012.

[15] S. R. Darr, H. Hu, N. G. Glikin et al., "An experimental study on terrestrial cryogenic transfer line chilldown I. Effect of mass flux, equilibrium quality, and inlet subcooling," *International Journal of Heat and Mass Transfer*, vol. 103, pp. 1225–1242, 2016.

[16] S. R. Darr, H. Hu, N. Glikin et al., "An experimental study on terrestrial cryogenic tube chilldown II. Effect of flow direction with respect to gravity and new correlation set," *International Journal of Heat and Mass Transfer*, vol. 103, pp. 1243–1260, 2016.

[17] S. R. Darr, J. W. Hartwig, J. Dong et al., "Two-phase pipe quenching correlations for liquid nitrogen and liquid hydrogen," *Journal of Heat Transfer*, vol. 141, no. 4, p. 4, 2019.

[18] J. Wang, Y. Li, L. Wang, K. Zhu, F. S. Xie, and C. Li, "Transient modeling of cryogenic two-phase flow boiling during chilldown process," *Applied Thermal Engineering*, vol. 143, pp. 461–471, 2018.

[19] J. Wang, Y. Li, L. Wang, H. Mao, Y. Ma, and F. S. Xie, "Experimental investigation on two-phase flow instabilities in long-distance transportation of liquid oxygen," *Cryogenics*, vol. 102, pp. 56–64, 2019.

[20] L. Wang, J. Wang, X. Huang et al., "Experimental investigation on cryogenic chilldown performance under high-Reynolds number condition and using interior micro-fin structure," *International Journal of Heat and Mass Transfer*, vol. 182, article 121979, 2022.

[21] W. Xu and P. Zhang, "Cryogenic quenching of a stainless steel rodlet with various coatings," *International Journal of Heat and Mass Transfer*, vol. 154, article 119642, 2020.

[22] W. Xu, C. Cheng, X. Song, and P. Zhang, "Experimental investigation of cryogenic flow quenching of horizontal stainless steel tubes," *Cryogenics*, vol. 117, article 103327, 2021.

[23] J. Hartwig, P. Meyerhofer, B. Stiegemeier, and R. Morehead, "Liquid methane and liquid oxygen horizontal chilldown experiments of a 2.54 and 11.43 cm transfer line," *Applied Thermal Engineering*, vol. 205, article 118042, 2022.

[24] S. R. Darr, H. Hu, R. Shaeffer, J. Chung, J. W. Hartwig, and A. K. Majumdar, "Numerical simulation of the liquid nitrogen chilldown of a vertical tube," in *53rd aiaa aerospace sciences meeting*, Kissimmee, Florida, 2015.

[25] J. Chen, R. Zeng, X. Zhang, L. Qiu, and J. Xie, "Numerical modeling of flow film boiling in cryogenic chilldown process using the AIAD framework," *International Journal of Heat and Mass Transfer*, vol. 124, pp. 269–278, 2018.

[26] J. C. Melcher and R. L. Morehead, "Combustion stability characteristics of the Project Morpheus liquid oxygen/liquid methane main engine," in *50th AIAA/ASME/SAE/ASEE Joint Propulsion Conference*, Cleveland, OH, 2014.

[27] M. Leonardi, F. Di Matteo, J. Steelant, F. Nasuti, and M. Onofri, "System analysis of low frequency combustion instabilities in liquid rocket engines," in *51st AIAA/SAE/ASEE Joint Propulsion Conference*, Orlando, FL, 2015.

[28] J. Zhang, K. Wang, and L. Chen, "Experimental study on liquid oxygen chilldown in the horizontal pipe with an injector on the exit," *Applied Thermal Engineering*, vol. 173, article 115212, 2020.

[29] J. Zhang, K. Wang, and L. Chen, "Characteristics of boiling transitions during liquid oxygen chill-down in a horizontal pipe with an injector on the exit," *Applied Thermal Engineering*, vol. 182, article 116068, 2021.

[30] J. Zhang, K. Wang, and L. Chen, "Experimental study on liquid oxygen chill-down in a horizontal exit-contracted pipe," *Cryogenics*, vol. 120, article 103387, 2021.

[31] J. Zhang, K. Wang, and L. Chen, "Fill-in and boiling transition characteristics during the liquid oxygen chill-down process in a vertical exit-contracted pipe," *International Journal of Aerospace Engineering*, vol. 2022, Article ID 5899199, 22 pages, 2022.

[32] P. J. Berenson, "Film-boiling heat transfer from a horizontal surface," *Journal of Heat Transfer*, vol. 83, no. 3, pp. 351–356, 1961.

[33] D. D. Hall and I. Mudawar, "Critical heat flux (CHF) for water flow in tubes–I. Compilation and assessment of world CHF data," *International Journal of Heat and Mass Transfer*, vol. 43, no. 14, pp. 2573–2604, 2000.

[34] K. Yuan, Y. Ji, and J. N. Chung, "Numerical modeling of cryogenic chilldown process in terrestrial gravity and microgravity," *International Journal of Heat and Fluid Flow*, vol. 30, no. 1, pp. 44–53, 2009.